nature cell biology

ARTICLES

https://doi.org/10.1038/s41556-018-0215-z

Deregulation of CRAD-controlled cytoskeleton initiates mucinous colorectal cancer via β-catenin

Youn-Sang Jung[1], Wenqi Wang[2], Sohee Jun[1], Jie Zhang[1], Mrinal Srivastava[1], Moon Jong Kim[1], Esther M. Lien[1], Joan Shang[1], Junjie Chen[1,3,4], Pierre D. McCrea[3,4,5], Songlin Zhang[6] and Jae-Il Park[1,3,4*]

Epithelial integrity is maintained by the cytoskeleton and through cell adhesion. However, it is not yet known how a deregulated cytoskeleton is associated with cancer. We identified cancer-related regulator of actin dynamics (*CRAD*) as frequently mutated or transcriptionally downregulated in colorectal cancer. We found that CRAD stabilizes the cadherin–catenin–actin complex via capping protein inhibition. The loss of CRAD inhibits F-actin polymerization and subsequently disrupts the cadherin–catenin–actin complex, which leads to β-catenin release and Wnt signalling hyperactivation. In mice, *CRAD* knockout induces epithelial cell integrity loss and Wnt signalling activation, resulting in the development of intestinal mucinous adenoma. With *APC* mutation, *CRAD* knockout initiates and accelerates mucinous and invasive adenoma development in the colorectum. These results define CRAD as a tumour suppressor, the inactivation of which deregulates the cytoskeleton and hyperactivates Wnt signalling thus initiating mucinous colorectal cancer. Our study reveals the unexpected roles of an actin cytoskeletal regulator in maintaining epithelial cell integrity and suppressing tumorigenesis.

Epithelial monolayer integrity is, to a significant extent, maintained through cell–cell adhesion, the cytoskeleton and basement membrane interaction[1–3]. Cell adhesion proteins and the cytoskeleton are intimately associated, with the E-cadherin–catenin complex and filamentous actin (F-actin) being prime examples. E-cadherin participates in cell adhesion and contact inhibition as part of a large complex composed of catenins and additional proteins (such as α-, β- and p120-catenin, vinculin, α-actinin and eplin) that is stabilized by interactions with F-actin[2–5]. F-actin polymerization, which involves the addition of ATP–globular actin (G-actin) at the barbed (or +) end of filaments, is controlled by capping proteins (CPs) and CP regulators[6]. CPs directly bind and block the barbed end of filaments or ATP–G-actin, resulting in the inhibition of actin assembly. Several CP regulators control CPs. For example, formins and Ena/VASP compete with CPs for actin binding[7,8]. Alternatively, V-1 and phospholipids bind to CPs and prevent interactions between CPs and actin[9,10]. Given that F-actin stabilizes the E-cadherin–catenin complex for the maintenance of epithelial cell integrity, we hypothesized that reduced epithelial cell integrity through the deregulation of the cytoskeleton and the E-cadherin–catenin complex contributes to tumorigenesis. Our unbiased and comprehensive approaches identified cancer-related regulator of actin dynamics (*CRAD*; *KIAA1211*) as a tumour suppressor in colorectal cancer (CRC).

CRAD is markedly mutated in small cell lung cancer patient samples, ranked as the third most frequently mutated gene after *TP53* and *RB1*[11]. Here, our comprehensive approaches reveal that *CRAD* inactivation initiates mucinous intestinal tumorigenesis by disrupting epithelial cell integrity.

CRAD inactivation in CRC

To identify potential tumour-suppressor genes that are specifically inactivated in CRC, we selected genes whose expression is significantly downregulated in CRC. Analysis of Oncomine datasets showed that the transcriptional level of *CRAD* was notably downregulated in CRC samples (Fig. 1a). Similarly, analysis of Gene Expression Omnibus (GEO) datasets indicated a significant downregulation of *CRAD* mRNA in CRC compared to the adjacent normal samples (Fig. 1b). Immunohistochemistry (IHC) of tissue microarrays (TMAs) also showed decreased CRAD in CRC (Fig. 1c and Supplementary Table 1). Furthermore, CRC cells exhibited reduced *CRAD* mRNA expression (Fig. 1d) and protein levels (Fig. 1e) compared to intestinal epithelial cells (IECs). In addition, *CRAD* alleles harbour nonsense mutations in CRC patient samples and CRC cell lines (Fig. 1f–h and Supplementary Fig 1). Interestingly, transcriptional downregulation of *CRAD* was observed in CRC cell lines without *CRAD* genetic mutations (Fig. 1d) but was restored with the inhibition of methyltransferase (Supplementary Fig. 1c). These results suggest that *CRAD* is inactivated by genetic mutation or transcriptional downregulation in CRC.

Positive regulation of actin polymerization by CRAD

Given the mutation or downregulation of *CRAD* in CRC, we hypothesized that *CRAD* is a tumour suppressor in CRC. To test this, we examined whether *CRAD* inactivation is involved in cell transformation-related cell morphological change[12], as reflected in the respective cell morphologies and actin distributions of IECs compared to CRC cell lines (Supplementary Fig. 2a,b). We found that *CRAD* depletion (Supplementary Fig. 2c,d) induced IEC shrinkage (Supplementary Fig. 2e,f), which was indicated by reduced cell areas and decreased phalloidin staining, a marker for F-actin (Supplementary Fig. 2g). Conversely, CRAD ectopic expression increased the cell area of CRC cells, with an elevated actin cytoskeleton (Supplementary Fig. 2h–k). These results suggest that CRAD positively regulates the actin polymerization.

[1]Department of Experimental Radiation Oncology, The University of Texas MD Anderson Cancer Center, Houston, TX, USA. [2]Department of Developmental and Cell Biology, University of California, Irvine, Irvine, CA, USA. [3]Program in Genetics and Epigenetics, The University of Texas MD Anderson Cancer Center, Houston, TX, USA. [4]Graduate School of Biomedical Sciences at Houston, The University of Texas Health Science Center and MD Anderson Cancer Center, Houston, TX, USA. [5]Department of Molecular Genetics, The University of Texas MD Anderson Cancer Center, Houston, TX, USA. [6]Department of Pathology, The University of Texas McGovern Medical School, Houston, TX, USA. *e-mail: jaeil@mdanderson.org

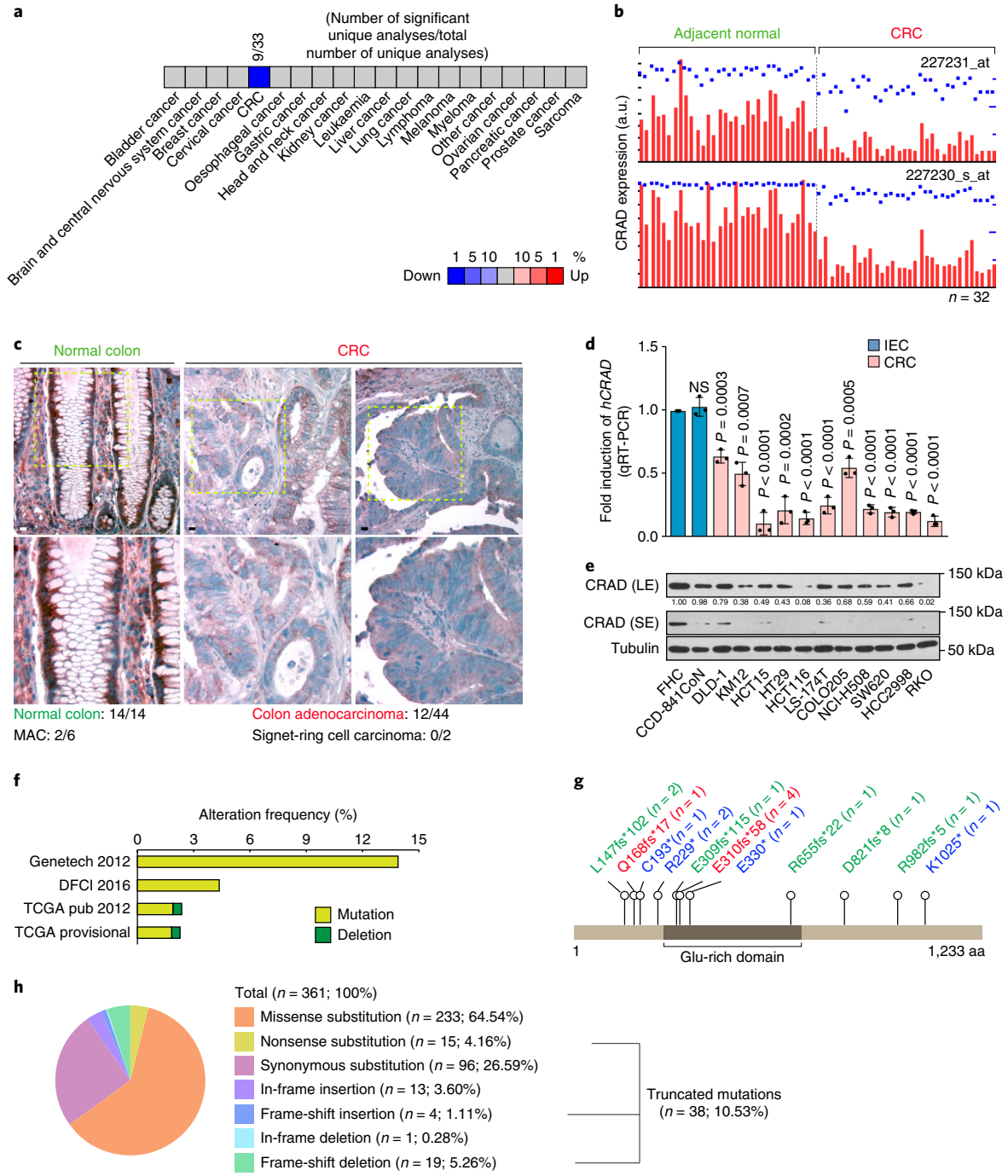

Fig. 1 | *CRAD* inactivation in CRC. a, Oncomine analysis of *CRAD* expression in human cancers. $P < 0.0001$; fold change > 2; gene rank = top 1%. **b**, GEO dataset (accession no. GDS2947) analysis of *CRAD* expression in adjacent normal tissues versus colorectal adenoma tissues ($n = 32$ patients; probes, 227231_at and 227230_s_at). Red bars indicate CRAD expression, blue dots indicate percentile rank within sample. **c**, Immunohistochemistry of CRAD in normal colon and CRC. The images are representative of 14 normal colon and 38 CRC samples. Yellow dashed boxes indicate region magnified in lower panels. MAC, human mucinous adenocarcinoma; Scale bars, 50 μm. **d**,**e**, Expression of CRAD in IECs and CRC cells analysed by quantitative reverse transcription-PCR (qRT-PCR; $n = 3$ independent experiments; **d**) and immunoblotting (**e**). Representative images from three independent immunoblotting experiments are shown; numbers indicate CRC expression of CRAD relative to EICs (normalized to FHC cells) as determined by ImageJ. *P* values from analysis of CRC cells versus IECs. **f**, Genetic alteration of *CRAD* determined for the cBioportal datasets: Genentech 2012 ($n = 72$ patient samples); TCGA pub 2012 ($n = 212$ patient samples); TCGA provisional ($n = 220$ patient samples) and DFCI 2016 ($n = 619$ patient samples). **g**,**h**, Catalogue of Somatic Mutations in Cancer (COSMIC) analysis of *CRAD* mutations in CRC. SE, short exposure; LE, long exposure; *n*, number of patient samples; error bars, mean ± s.d.; NS, not significant ($P > 0.05$); two-sided unpaired *t*-test.

CRAD as an inhibitor of CPs

Given the enhancement of the actin cytoskeleton by CRAD, we sought to dissect its detailed molecular mechanism. By employing tandem affinity purification and mass spectrometry, we identified CRAD-interacting proteins: CPs, actin/tubulin-associated proteins and the Arp2/3 protein complex (Fig. 2a and Supplementary Table 2). The

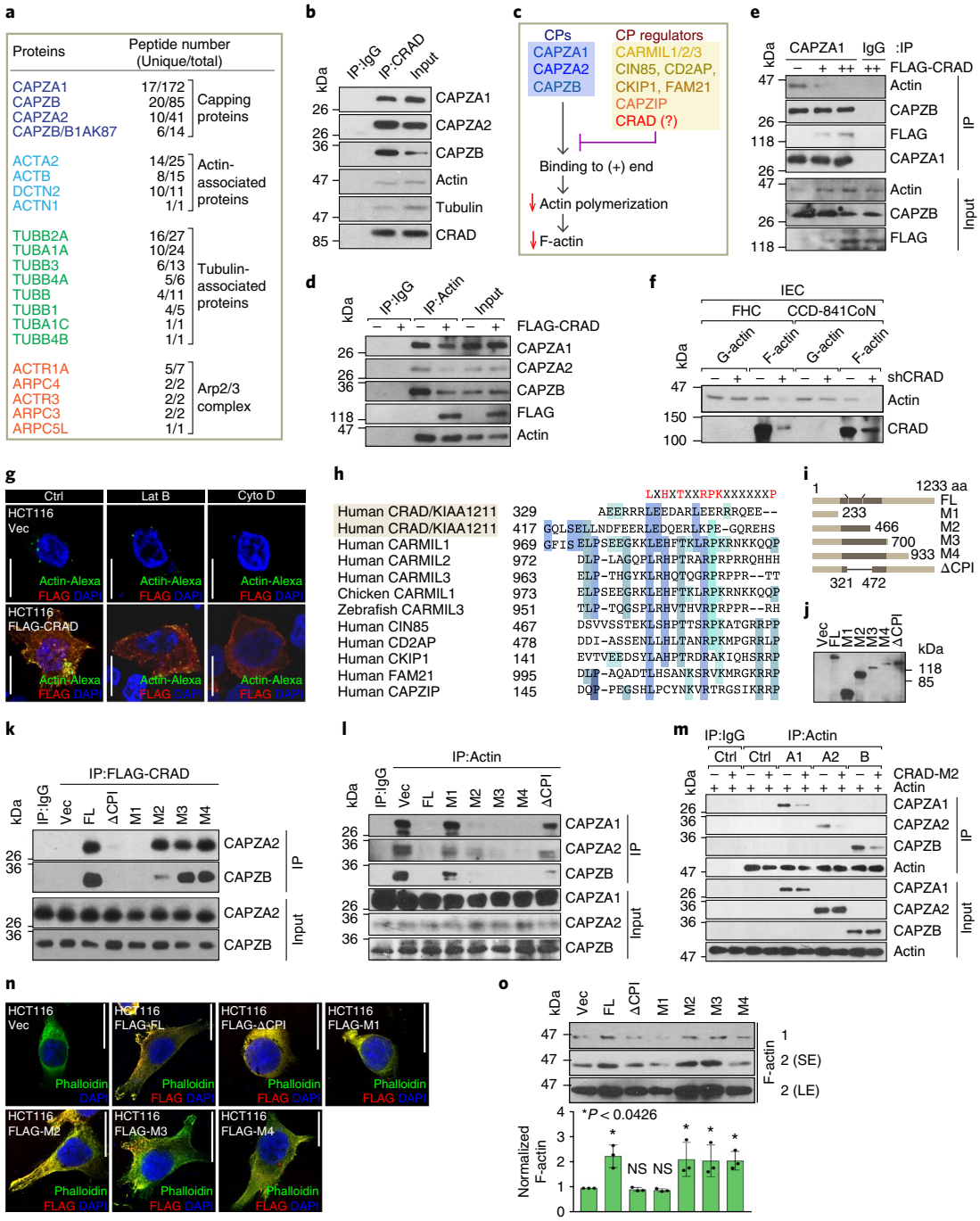

Fig. 2 | Positive regulation of the actin polymerization by CRAD-inhibited CPs. a, CRAD-interacting proteins identified by tandem affinity purification and mass spectrometry (see Supplementary Table 2). Tandem affinity purification and mass spectrometry was performed once. **b**, Endogenous interaction of CRAD with the CPs, actin and tubulin. FHC cell lysates were analysed for co-immunoprecipitation (IP). **c**, Illustration of the hypothetical model of CRAD-induced actin polymerization. **d**,**e**, Decreased interaction between CPs and actin by CRAD. The reciprocal co-IP analysis of HCT116 cells transfected with FLAG-CRAD plasmid with either actin (**d**) or CAPZA1 antibodies (**e**) is shown. **f**, Decreased F-actin by CRAD depletion in IECs. Fractionation and immunoblotting assays of F-/G-actin. **g**, Increase in uncapped barbed ends by CRAD. Cells were permeabilized by saponin-containing buffer for the visualization of uncapped barbed ends using a Super Resolution microscope. The images are representative of two independent experiments ($n = 3$ independent samples in each) with similar results. **h**, Comparative amino acid sequence analysis of potential CPI motifs in CRAD with those in known CP regulators. **i**,**j**, The generation of CRAD-mutant constructs (**i**) and immunoblotting assays (**j**). Immunoblotting was performed once. **k**,**l**, CRAD–CP binding via CPI motifs. Reciprocal co-IP analysis of HCT116 cell lysates transfected with FLAG–CRAD (full-length (FL), ΔCPI and M1–M4) plasmids, with either FLAG (**k**) or actin antibodies (**l**). Vec, vector. **m**, Decreased interaction between CAPZs and actin by CRAD. Direct binding and blocking were analysed by co-IP assays using purified recombinant proteins. **n**,**o**, The increase of F-actin formation by ectopic expression of CPI motifs-containing CRAD mutants. **n**, After 24 h transfection with each plasmid, HCT116 CRC cells were visualized by phalloidin immunofluorescence staining. Images are representative of three independent experiments ($n = 3$ independent samples in each) with similar results. **o**, Cells were fractionated into F-actin and G-actin and analysed by immunoblotting (top) and normalized by G-actin expression using ImageJ (bottom). Data in panels **b**, **d**–**f**, **k**–**m** and **o** are from three independent experiments. Scale bars, 20 μm; error bars, mean ± s.d.; NS, not significant ($P > 0.05$); two-sided unpaired *t*-test; IP, immunoprecipitation; Ctrl, control.

capping proteins CAPZA1, CAPZB and CAPZA2 exhibited high scores with regards to peptide numbers. Co-immunoprecipitation (co-IP) from cell lysates and pull-down assays of purified proteins validated the endogenous and direct interaction between CRAD and the CPs (Fig. 2b and Supplementary Fig. 2l). Thus, we hypothesized that CRAD enhances F-actin polymerization by inhibiting CPs (Fig. 2c). We examined whether CRAD interferes with the binding of CPs to actin. Co-immunoprecipitation assays showed that ectopic CRAD reduced the interaction between CPs and actin (Fig. 2d,e). F-actin controls the cytoskeletal dynamics and stretched cell morphologies (Supplementary Fig. 2e–k)[13–15]. For F-actin assembly, monomeric G-actin undergoes polymerization at the barbed end through a conformational change, represented by the high ratio of F-actin to G-actin. Fractionation of F-/G-actin indicated a decrease in F-actin levels in *CRAD*-depleted IECs (Fig. 2f and Supplementary Fig. 2m). Conversely, CRAD ectopic expression increased F-actin in CRC cells (Supplementary Fig. 2n,o), which is consistent with the phalloidin staining. Having determined that CPs directly bind to the barbed end of F-actin and inhibit F-actin polymerization[6], we next investigated whether CRAD sequesters CPs from F-actin and increases the uncapped barbed ends of F-actin. Visualization of the uncapped barbed ends[16] showed that the ectopic expression of CRAD led to an increase in uncapped barbed ends (Fig. 2g). In addition, highly expressed CRAD increased the uncapped barbed ends in the Latrunculin B (Lat B; an inhibitor of monomeric G-actin)-treated condition but not in the Cytochalasin D (Cyto D; a blocker of barbed end)-treated condition (Fig. 2g). These results suggest that CRAD-upregulated actin polymerization is mainly due to the increase of the extendable barbed ends by inhibiting CPs, independently of the increase of monomeric G-actin. Direct CP regulators, including CARMILs, FAM21 and CD2AP, harbour a CP interaction (CPI) motif[5]. Interestingly, CRAD also contains two potential CPI motifs at amino acid residues 329 and 417 (Fig. 2h). To determine whether these predicted CPI motifs in CRAD are required for CP inhibition, we constructed CRAD mutants (M1–M4 and ΔCPI; Fig. 2i,j). Co-immunoprecipitation showed that, unlike full-length and M2–M4 mutants, M1 and ΔCPI mutants (lacking CPI motifs) did not bind to CPs (Fig. 2k) and failed to inhibit the interaction of CPs with actin (Fig. 2l). In vitro protein binding assays using the purified proteins of actin, CPs and CRAD-M2 (Supplementary Fig. 2p) also showed that CRAD inhibited actin–CP binding (Fig. 2m and Supplementary Fig.2q). Moreover, in CRC cells, M1 and ΔCPI mutants failed to induce a stretched cell morphology (Fig. 2n) and F-actin polymerization (Fig. 2o) unlike other mutants (M2–M4; Fig. 2n,o). These data suggest that CRAD downregulates the interaction between CPs and the barbed ends via the CPI motifs in CRAD, which increases F-actin polymerization (Supplementary Fig. 3).

CRAD loss-activated Wnt signalling by disrupted CCA complex

We next sought to determine CRAD-modulated actin cytoskeletons are associated with intestinal tumorigenesis. Owing to the deregulation of various developmental pathways in CRC, we examined the effects of CRAD on Wnt, Hedgehog, BMP, Notch and Hippo signalling. Interestingly, CRAD overexpression downregulated Wnt/β-catenin target genes (*AXIN2* and *CD44*; Fig. 3a). Conversely, in IECs, *CRAD* depletion augmented Wnt/β-catenin target-gene expression (Fig. 3b). In addition, *CRAD* expression is mutually exclusive to the expression of *AXIN2* in CRC (Supplementary Fig. 4a). The level of nuclear β-catenin in IECs and CRC cell lines was consistently inversely correlated with the expression of CRAD (Fig. S4b). These results imply that CRAD might be negatively associated with Wnt/β-catenin signalling. Indeed, CRAD depletion increased β-catenin reporter activity, *AXIN2* expression and the level of active β-catenin in IECs (Fig. 3c–e). Importantly, the treatment of cells with iCRT14, an inhibitor of β-catenin-TCF binding, suppressed *CRAD* depletion-induced β-catenin reporter activation (Fig. 3f). Also, Engrailed-LEF1 (Eng-LEF1), a dominant-negative mutant blocking β-catenin-mediated gene activation[17], suppressed *AXIN2* upregulation in *CRAD*-depleted IECs (Fig. 3g). These results indicate that CRAD knockdown-induced upregulation of the β-catenin reporter and target genes is due to β-catenin-mediated transcriptional activation.

To complement this, we examined the effects of CRAD ectopic expression on Wnt/β-catenin signalling in CRC cells. CRAD expression suppressed β-catenin reporter activity, *AXIN2* and active β-catenin (Fig. 3h–j). Moreover, the M1 and ΔCPI constructs failed to downregulate *AXIN2* (Fig. 3k), which suggests that the CPI motifs in CRAD are required for the suppression of β-catenin target-gene activation.

Catenin proteins connect E-cadherin to the actin cytoskeleton, which contributes to the maintenance of epithelial cell integrity through cell–cell adhesion[4,5,18,19] and downregulates the nuclear translocation of catenins[20]. Given the role of CRAD in modulating the actin cytoskeleton (Fig. 2), we investigated whether CRAD has an impact on the interaction between catenins and E-cadherin. In IECs, CRAD knockdown increased the levels of β -catenin and α-catenin both in the cytosol and the nucleus (Fig. 3l and Supplementary Fig. 4c). Conversely, CRAD expression decreased nuclear β-catenin in HCT116 CRC cells (Fig. 3m and Supplementary Fig. 4d) and co-IP assays showed that CRAD knockdown reduced the interaction between E-cadherin and catenin proteins (Fig. 3n and Supplementary Fig. 4e). In CRC cells, however, CRAD overexpression induced the binding of catenin proteins with E-cadherin (Fig. 3o and Supplementary Fig. 4f). Super Resolution microscopic analyses also showed that CRAD-expressing HCT116 cells displayed increased β-catenin associated with E-cadherin in cell–cell adhesion (Fig. 3p and Supplementary Fig. 4g). Given that the actin cytoskeletal dynamics modulate E-cadherin-mediated cell adhesion[5,18,21], we investigated whether CRAD-modulation of the actin cytoskeleton affects E-cadherin–catenin binding. Duolink (Fig. 3q) and co-IP assays showed that the ectopic expression of the full-length and M2–M4 mutants stabilized the E-cadherin–catenin complex, whereas M1 and ΔCPI mutants did not (Fig. 3r,s). We also verified β-catenin transcriptional activity under conditions of actin-cytoskeletal inhibition versus stabilization. Actin polymerization inhibitors (Lat B and Cyto D) increased the transcriptional activity of β-catenin, whereas an F-actin stabilizer (Jasplakinolide) reduced it (Supplementary Fig. 4h,i). These results suggest that under normal conditions, CRAD enhances the actin polymerization through CP inhibition, which stabilizes the cadherin–catenin–actin (CCA) complex. Conversely, after CRAD inactivation, a diminished actin cytoskeleton destabilizes the CCA complex. This releases β-catenin from the cadherin, followed by nuclear translocation of β-catenin and activation of Wnt/β-catenin target genes (Supplementary Fig. 4j).

Inhibition of CRC cell proliferation by CRAD

Having observed the inactivation of *CRAD* in CRC (see Fig. 1) and CRAD inactivation-induced Wnt/β-catenin signalling activation, we next determined the effects of CRAD on IEC and CRC cell proliferation. Given the high expression of CRAD in IECs, we depleted endogenous *CRAD* in IECs using short hairpin RNA (shRNA). The knockdown of CRAD increased IEC proliferation (Fig. 4a), which was reversed by iCRT14 (Fig. 4b and Supplementary Fig. 5a,b) or Eng-LEF1 (Fig. 4c and Supplementary Fig. 5c–e). These data indicate that CRAD depletion-induced IEC hyperproliferation is mediated by β-catenin target-gene activation. Conversely, CRAD overexpression inhibited CRC cell proliferation (Fig. 4d and Supplementary Fig. 5f–h), which was rescued by β-catenin (Fig. 4e and Supplementary Fig. 5i–o). These results suggest that CRAD-induced CRC cell growth inhibition is mainly due to the suppression of β-catenin signalling. Furthermore, unlike the

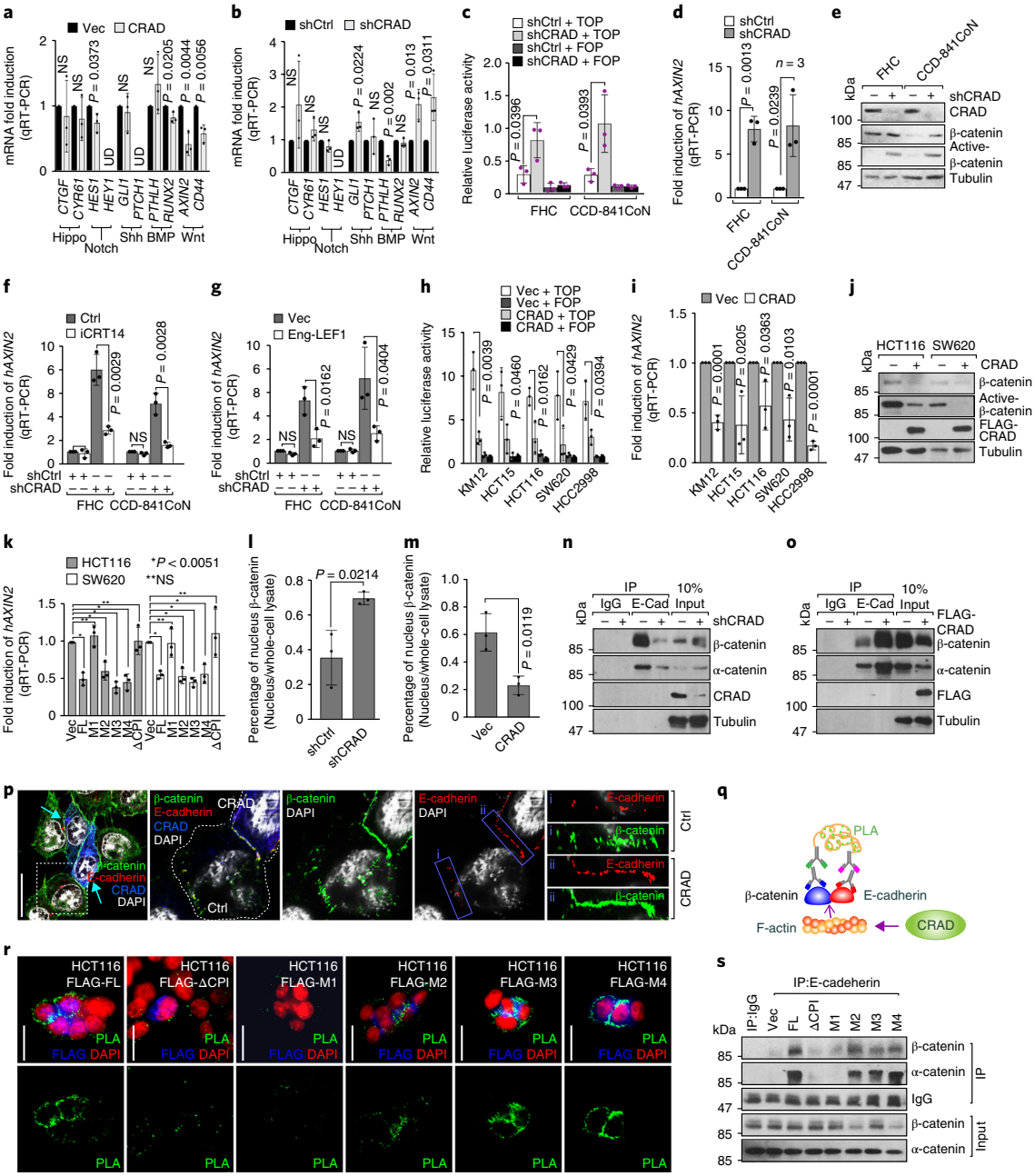

Fig. 3 | Loss of CRAD-activated Wnt signalling through disruption of the CCA complex. a, Decreased expression of Wnt-signalling target genes by CRAD ectopic expression. HCT116 cells were analysed by qRT-PCR 24 h after transfection. **b**, Increased expression of Wnt-signalling target genes by CRAD knockdown. CRAD-depleted CCD-841CoN cells were analysed by qRT-PCR. Shh, sonic hedgehog signalling. **c**,**d**, Increased β-catenin transcriptional activity by CRAD depletion. **c**, Intestinal epithelial cells were transfected with β-catenin reporter plasmids (TOP/FOPFLASH) for the luciferase assays. **d**, Quantitative reverse transcriptase-PCR of *AXIN2*. **e**, Immunoblot assays showing increased β-catenin protein as a result of CRAD depletion in IECs. **f**,**g**, Inhibition of CRAD depletion-induced *AXIN2* upregulation by iCRT14 (**f**) or Eng-LEF1 (**g**). Intestinal epithelial cells were analysed by qRT-PCR 24 h after iCRT14 (100 μM) treatment or Eng-LEF1 transient transfection. **h–j**, Suppression of β-catenin transcriptional activity by CRAD in CRC cells. Twenty-four hours after transfection, CRC cells were analysed by means of TOP/FOPFLASH luciferase analysis (**h**), qRT-PCR of *AXIN2* (**i**) and immunoblotting for β-catenin (**j**). The experiment was performed once. **k**, Inhibition of β-catenin target-gene expression by CPI motif-containing CRAD mutants. CRC cells were analysed for TOP/FOPFLASH luciferase activity 24 h after transfection. **l**, Decreased nuclear β-catenin by CRAD overexpression. Intestinal epithelial cells (**l**) and CRC cells (**m**) were transfected with shCtrl or shCRAD and Vec or CRAD, respectively. After 48 h, the cells were fractionated into the cytosolic and nuclear fractions and immunoblotted. Nuclear β-catenin was quantified using ImageJ. **n**, Decreased interaction between E-cadherin and catenins following CRAD depletion. Co-IP assays of shCRAD–CCD-841CoN. Representative images from three independent experiments with similar results are shown. **o**,**p**, Increased interaction between E-cadherin and catenins by CRAD. HCT116 cells were transfected with FLAG-CRAD plasmid. **o**, Co-IP assays. **p**, Immunofluorescence staining. The arrows indicate CRAD-expressing cells. In comparison to non-transfected cells (i), CRAD-expressing cells (ii) displayed increased colocalization of E-cadherin and β-catenin. Representative images from three independent experiments with similar results are shown. **q**, Illustration of E-cadherin–β-catenin binding analysis using Duolink assays. **r**,**s**, Restoration of E-cadherin–β-catenin binding by CPI motif-containing CRAD mutants in CRC cells. **r**, Duolink assay. Green fluorescence (proximity ligation assay; PLA) indicates E-cadherin–β-catenin interaction. **s**, Co-IP analysis. Representative images of three experiments with similar results are shown. Data in panels **a**–**h** and **k**–**m** are from three independent experiments. Scale bars, 20 μm; error bars, mean ± s.d.; NS, not significant ($P > 0.05$); two-sided unpaired *t*-test; UD, undetected.

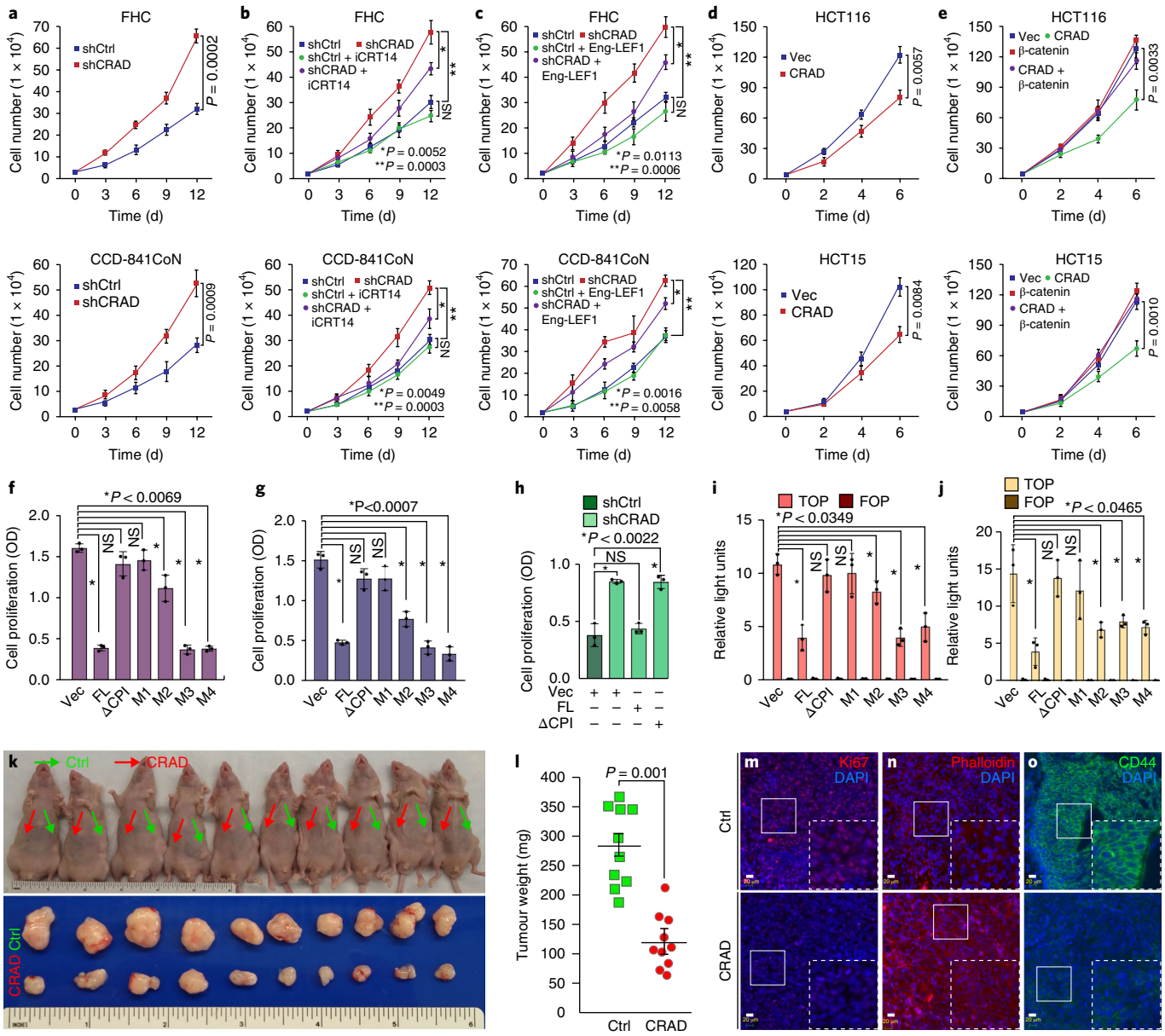

Fig. 4 | Inhibition of CRC cell proliferation by CRAD. a, Hyperproliferation of IECs after CRAD depletion. The proliferation of FHC and CCD-841CoN cells transfected with shCtrl or shCRAD was analysed by cell counting. **b**,**c**, Suppression of shCRAD-induced cell hyperproliferation by β-catenin inhibition in IECs. **b**, FHC and CCD-841CoN cells (shCtrl and shCRAD transfected) were treated with iCRT14 (100 μM) for 14 d and cells were counted. **c**, Intestinal epithelial cells (shCtrl and shCRAD) were transfected with Eng-LEF1 and cell proliferation was analysed. **d**, CRC cell growth inhibition by CRAD expression. The cell proliferation of HCT116 and HCT15 cells (Vec (control) and CRAD-expressing) was analysed. **e**, CRAD-induced CRC cell growth inhibition is rescued by β-catenin. HCT116 and HCT15 cells were transfected with CRAD or β-catenin plasmids and cell proliferation was analysed. **f**–**h**, CRC cell growth inhibition by CPI motif-containing CRAD mutants. The cell proliferation of CRAD (full-length, ΔCPI and M1–M4)-transfected CRC cells, HCT116 (**f**) and SW620 cells (**g**), was analysed. **h**, CCD-841CoN cells were transfected with each plasmid and the cell proliferation was analysed. **i**,**j**, Suppression of β-catenin reporter by CPI motif-containing CRAD mutants. HCT116 (**i**) and SW620 (**j**) cells transfected with CRAD full-length or mutant constructs were analysed for luciferase activity. **k**–**o**, Inhibition of ex vivo tumour development by CRAD. HCT116 control and HCT116-CRAD cells were subcutaneously injected into the left (green arrows) and right (red arrows) mouse flank, respectively (**k**, lower panel indicates isolated tumours from each mouse), and analysed for tumour weight (**l**; $n = 10$ mice) and IHC (**m**–**o**) using Ki67 (**m**), phalloidin (**n**) and CD44 (**o**). White boxes indicate regions magnified in dashed boxes. The experiments in **k** and **l** were performed once. Data in **a**–**j** and **o** are from three independent experiments. Scale bars, 20 μm; error bars, mean ± s.d.; NS, not significant ($P > 0.05$); two-sided unpaired *t*-test.

full-length and M2–M4 mutants, the ΔCPI and M1 constructs did not inhibit CRC cell proliferation (Fig. 4f,g and Supplementary Fig. 5p,q). Importantly, CRAD depletion-induced IEC hyperproliferation was reverted by the expression of the full-length mutant, but not by expression of the ΔCPI mutant (Fig. 4h). Similarly, β-catenin reporter activity was downregulated by the full-length and M2–M4 mutants but not by the ΔCPI or M1 mutants (Fig. 4i,j). These results suggest that the CPI motifs of CRAD are required to inhibit CRC cell proliferation.

Furthermore, xenograft transplantation assays showed that, compared to HCT116, HCT116-CRAD injected mice exhibited reduced tumour development (Fig. 4k,l), with notably decreased

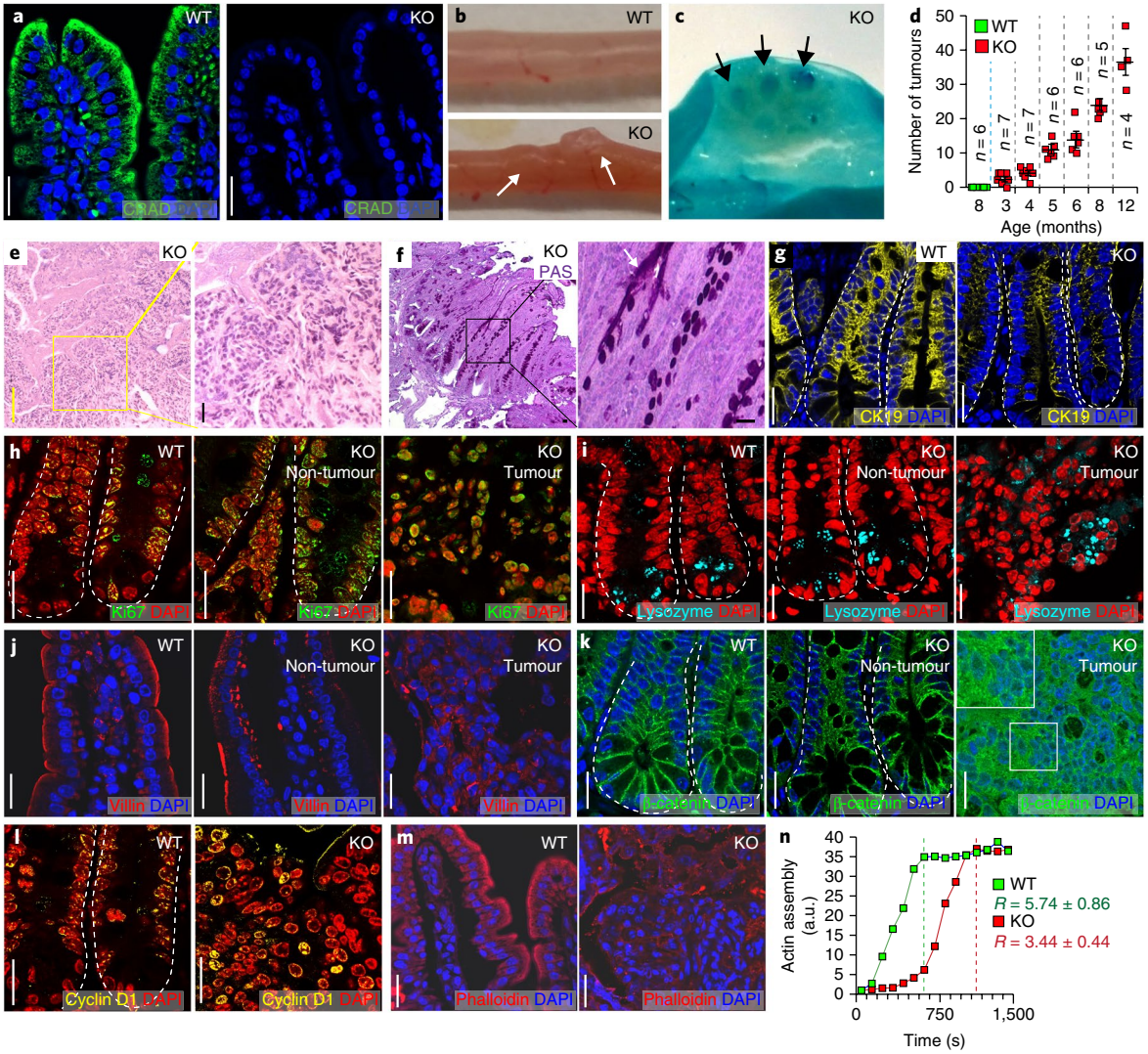

Fig. 5 | Intestinal adenoma development induced by *CRAD* KO. a, CRAD expression in the mouse small intestine. The *CRAD* KO mouse serves as a negative control in the IHC experiment. **b**,**c**, Intestinal adenoma development in *CRAD* KO mice. **b**, Adenomas in the small intestine of *CRAD* KO mice (3 months old). **c**, Methylene blue staining. The arrows in **b** and **c** indicate intestinal adenoma. **d**, Age-dependent intestinal adenoma development in *CRAD* KO mice. The numbers of mice are indicated. Error bars, mean ± s.d. The experiment was performed once. **e**, Intestinal adenoma (*CRAD* KO) stained with H&E. Yellow box shows the magnified image. Yellow and black scale bars, 100 μm and 20 μm, respectively. **f**, PAS-stained intestinal adenoma in *CRAD* KO mice. Black box shows the magnified image. Arrow indicates mucin deposition. **g**, Disruption of epithelial cell integrity. **h**, Cell hyperproliferation in the *CRAD* KO small intestine. IHC for Ki67. **i**, Abnormal differentiation of IECs in *CRAD* KO. The small intestine of WT and *CRAD* KO mice were immunostained with lysozyme. **j**, Disorganized cell adhesion in *CRAD* KO mice. Cells were stained with villin. **k**, Increased β-catenin in *CRAD* KO tumour. **l**, Upregulation of β-catenin target genes in the intestinal adenoma of *CRAD* KO mice. IHC for cyclin D1. **m**, Disorganized actin cytoskeleton in *CRAD* KO-induced tumour. F-actin was visualized by phalloidin staining. **n**, Decreased actin polymerization in *CRAD* KO mice. Cell extracts from the small intestine were analysed using actin polymerization assays from three independent experiments. The *R* values indicate the velocity of actin assembly. Representative images of three mice per group are shown. Scale bars, 20 μm unless specified; a.u., arbitrary unit.

cell proliferation, increased F-actin and downregulated β-catenin target genes (Fig. 4m–o). These in vitro and ex vivo results suggest that CRAD inhibits CRC proliferation through the suppression of β-catenin.

Intestinal adenoma development due to *CRAD* knockout

To address the in vivo consequence of *CRAD* gene inactivation in CRC, we established a *CRAD* knockout (KO) mouse model (Fig. 5a and Supplementary Fig. 6a–d). Importantly, *CRAD* KO mice displayed adenoma development in the small intestine (Fig. 5b,c) in an age-dependent manner (Fig. 5d). In addition, we found that *CRAD* KO mice showed decreased expression of Wnt/β-catenin target genes without the alteration of other signallings (Supplementary Fig. 6e). Intriguingly, *CRAD* KO mice also developed pulmonary lesions resembling early small cell lung cancer and solid-pseudopapillary neoplasm of the pancreas (Supplementary Fig. 6f,g). These results are supported by previous studies that show high mutation rates of *CRAD* in small cell lung cancer[11] and the constitutively active mutation of β-catenin in solid-pseudopapillary neoplasm of the pancreas[22]. Interestingly, mucin deposition in *CRAD* KO-induced intestinal adenoma was observed by hematoxylin and eosin (H&E) staining and periodic acid-Schiff (PAS) staining (Fig. 5e,f). Moreover, *CRAD* KO tumours displayed a heterogeneous loss of epithelial cell integrity (H&E and Cytokeratin 19

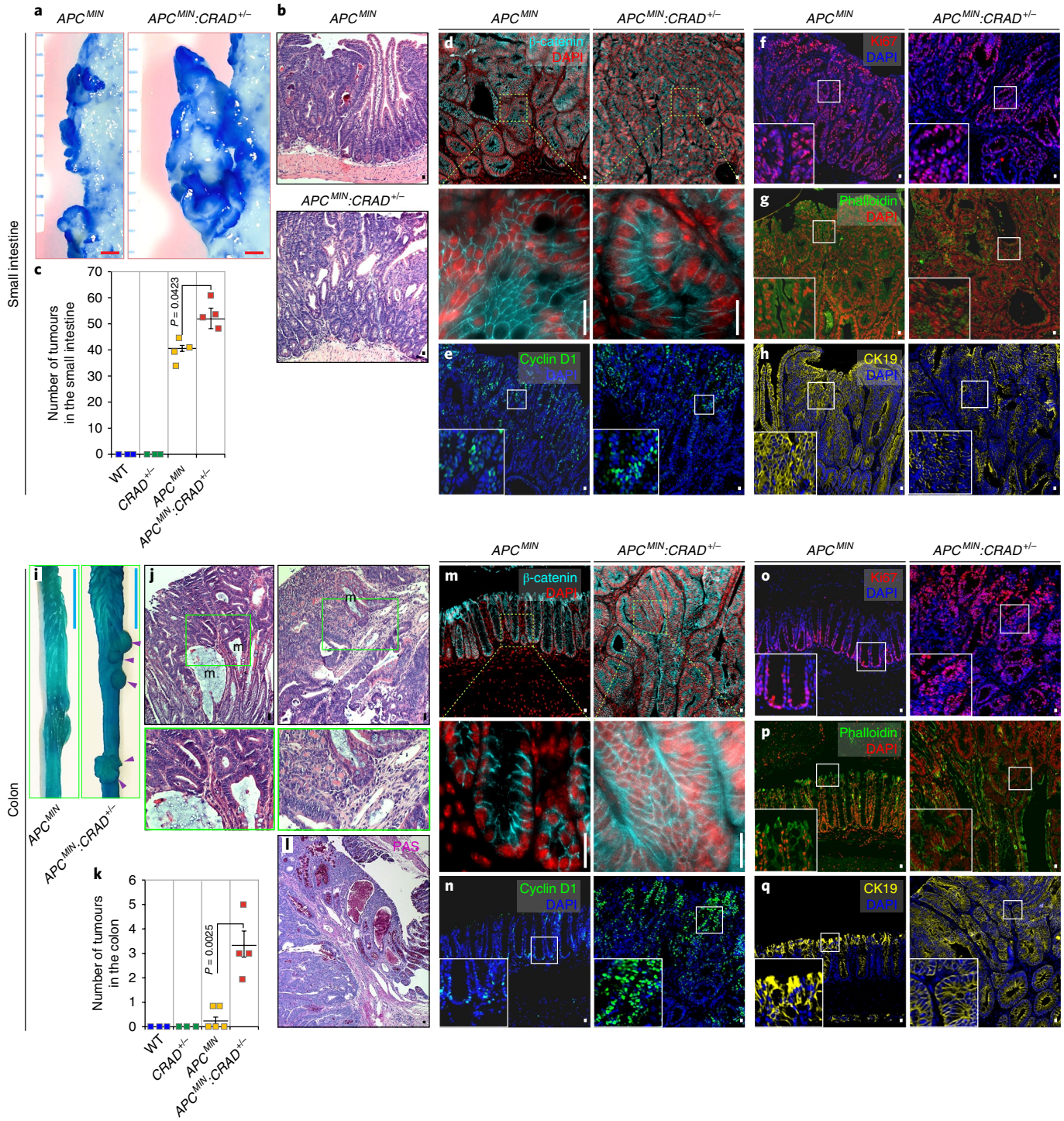

Fig. 6 | Accelerated intestinal tumorigenesis as a result of *CRAD* heterogeneous KO. a, Representative images of intestinal tumours from the small intestine of four-month old *APC*^{MIN} and *APC*^{MIN}:*CRAD*$^{+/-}$ mice ($n=4$ each). **b**,**c**, Increased numbers of small intestinal tumours in *APC*^{MIN}:*CRAD*$^{+/-}$ compared to *APC*^{MIN} mice ($n=4$ each). **b**, Representative H&E images of small intestinal tumours in *APC*^{MIN} and *APC*^{MIN}:*CRAD*$^{+/-}$ mice. **c**, Quantification of adenomas. **d**–**h**, Immunohistochemical staining of intestinal tumours from the small intestine of *APC*^{MIN} and *APC*^{MIN}:*CRAD*$^{+/-}$ mice. **d**, β-catenin. **e**, Cyclin D1. **f**, Ki67. **g**, Phalloidin. **h**, CK19. **i**, Colorectal tumours in four-month old *APC*^{MIN}:*CRAD*$^{+/-}$ mice ($n=4$ mice; arrowheads). **j**, H&E staining of the colorectal tumours in four-month old *APC*^{MIN}:*CRAD*$^{+/-}$ mice ($n=3$). m, mucin-accumulated lesion. **k**, Comparative analysis of colorectal tumours in four-month old WT ($n=3$), *CRAD*$^{+/-}$ ($n=3$), *APC*^{MIN} ($n=5$) and *APC*^{MIN}:*CRAD*$^{+/-}$ ($n=4$) mice. **l**, PAS-stained colorectal tumours in *APC*^{MIN}:*CRAD*$^{+/-}$ mice. **m**–**q**, Immunohistochemical staining of colorectal tumours from four-month old *APC*^{MIN} and *APC*^{MIN}:*CRAD*$^{+/-}$ mice. **m**, β-catenin. **n**, Cyclin D1. **o**, Ki67. **p**, Phalloidin. **q**, CK19. Images in panels **b**, **d**–**h**, **j** and **l**–**q** are representative of IHC experiments from three independent tumours. Dashed yellow, green and white boxes indicate magnified regions. Red scale bars, 1 mm; blue scale bars, 10 mm; black and white scale bars, 20 μm; error bars, mean ± s.d.; two-sided unpaired *t*-test.

(CK19) staining; Fig. 5e,g and Supplementary Fig. 6h). Loss of epithelial cell integrity is known to induce mucosal secretion and intestinal inflammation[23]. It should be noted that *CRAD* KO mice displayed a slight increase in intestinal inflammation

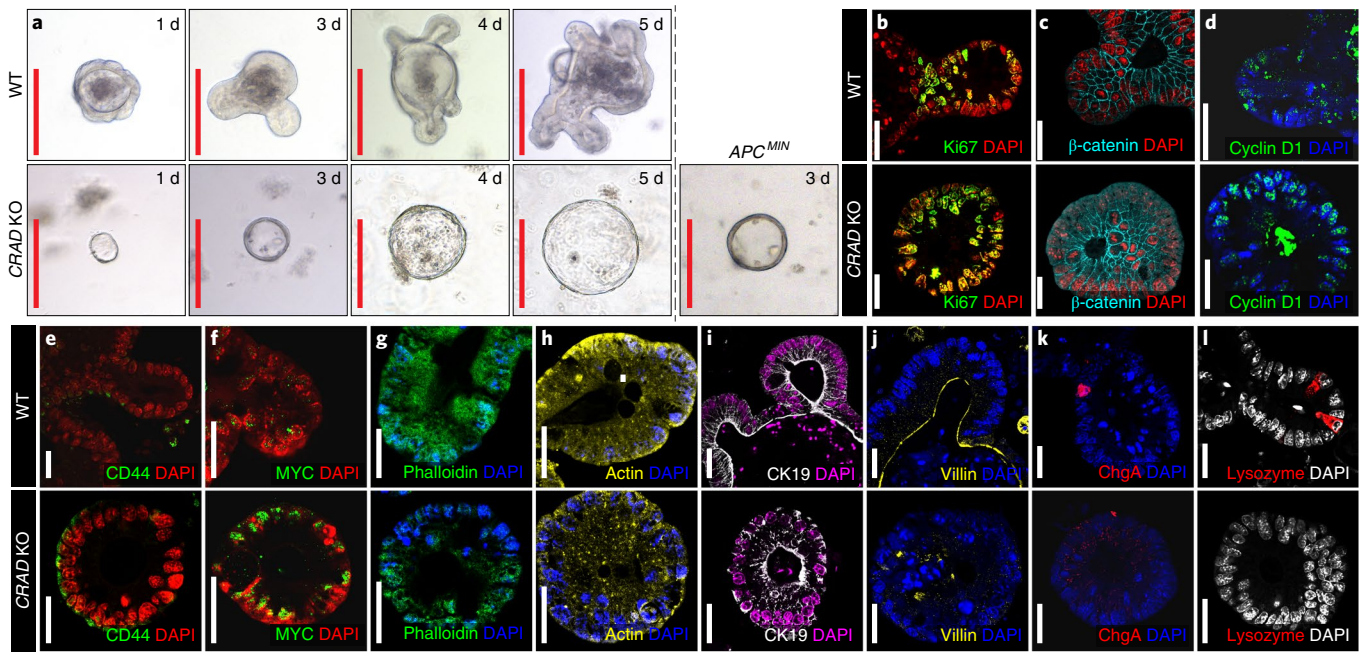

Fig. 7 | Mucinous intestinal tumorigenesis by *CRAD* KO. a, Cystic spheroids formation by *CRAD* KO. Isolated crypts from WT, *CRAD* KO and APC^{MIN} mice were maintained in the organoid culture medium. These data are representative of three independent organoid experiments with similar results. Ten organoids per group (total 50 organoids per WT and KO) were analysed. **b–l**, Immunohistochemical analysis of the organoids derived from *CRAD* WT and KO mouse intestine. Compared to WT, *CRAD* KO-driven cystic spheroids showed an increase in cell proliferation (Ki67; **b**), β-catenin (**c**) and its target genes (cyclin D1 (**d**), CD44 (**e**) and MYC (**f**)); disruption of the actin cytoskeleton (phalloidin (**g**) and actin (**h**)); loss of epithelial cell integrity (CK19 (**i**) and villin (**j**)) and decreased IEC lineage differentiation (Chromogranin A (ChgA; **k**) and lysozyme (**l**)). The images are representative of three experiments. Red scale bars, 20 μm; white scale bars, 20 μm.

(Fig. S6i,j). We also observed cell hyperproliferation in *CRAD* KO mice, indicated by elevated numbers of Ki67- and phospho-Histone H3-positive cells (Fig. 5h and Supplementary Fig. 6k–n) without notable differences in cell death (Supplementary Fig. 6o). Furthermore, IHC results for lysozyme (Paneth cells) and chromogranin A (neuroendocrine cells) indicated an increase in Paneth cells and a decrease in neuroendocrine cells in the *CRAD* KO intestine (Fig. 5i and Supplementary Fig. 6p), which might be because canonical Wnt signalling induces Paneth cell differentiation[24]. Given that CRAD depletion activates Wnt/β-catenin signalling by disrupting the CCA complex (see Fig. 3), we also examined cell–cell adhesion. *CRAD* KO mice showed the disorganized localization of E-cadherin and villin (Fig. 5j and Supplementary Fig. 6q). In addition, β-catenin and its target genes were upregulated in *CRAD* KO mice (Fig. 5k,l and Supplementary Fig. 6r) and *CRAD* KO-induced intestinal tumours exhibited disorganized and decreased levels of F-actin (Fig. 5m). Moreover, compared to wild type (WT), intestinal extracts from the *CRAD* KO mice showed a delayed rate in actin polymerization (Fig. 5n). These results strongly suggest that *CRAD* KO per se is sufficient to initiate intestinal tumorigenesis with the loss of epithelial cell integrity and the aberrant activation of Wnt/β-catenin signalling.

Accelerated intestinal tumorigenesis by *CRAD* KO

Given that *CRAD* gene mutations are often heterozygous in CRC patients (Supplementary Fig. 7a), we investigated whether genetic ablation of one allele of *CRAD* is associated with intestinal tumorigenesis. Compared to the APC^{MIN} strain, APC^{MIN}:$CRAD^{+/-}$ mice exhibited an increase in tumour numbers in the small intestine (Fig. 6a–c) without a change in β-catenin or cell proliferation (Fig. 6d–f). Furthermore, unlike adenomas from APC^{MIN}, tumours of APC^{MIN}:$CRAD^{+/-}$ mice displayed a loss of both F-actin (Fig. 6g) and epithelial cell properties (Fig. 6h), as observed in *CRAD* KO mice (see Fig. 5g,m).

Whereas APC^{MIN} mice develop tumours mainly in the small intestine but not in the colorectum[25], APC^{MIN}:$CRAD^{+/-}$ compound mice displayed severely invasive and mucinous adenomas in the colon (Fig. 6i–k). Intriguingly, colonic tumours of APC^{MIN}:$CRAD^{+/-}$ mice showed a marked increase in mucin accumulation (Fig. 6l), similar to human mucinous adenocarcinoma (MAC)[26]. Colonic adenomas from APC^{MIN}:$CRAD^{+/-}$ mice also exhibited significant upregulation of β-catenin (Fig. 6m), cyclin D1 (Fig. 6n and Supplementary Fig. 7b,c) and cell hyperproliferation (Fig. 6o and Supplementary Fig. 7d,e). Consistent with tumours in the small intestine, the heterogeneous loss of both F-actin and CK19 was also observed in colonic tumours of APC^{MIN}:$CRAD^{+/-}$ mice (Fig. 6p,q). Moreover, we observed the invasive adenoma development in APC^{MIN}:$CRAD^{+/-}$ mice, represented by the disruption of the basal membrane (Supplementary Fig. 7f). It should be noted that both APC^{MIN} and APC^{MIN}:$CRAD^{+/-}$ mice did not express mesenchymal markers (Supplementary Fig. 7g), which implies that epithelial–mesenchymal transition might not be involved in invasive tumour development in APC^{MIN}:$CRAD^{+/-}$ mice. These results suggest that, in conjunction with *APC* inactivation, the deletion of a *CRAD* allele leads to intestinal tumorigenesis in both the small and large intestine, which reveals a pathologic outcome of *CRAD* heterozygous mutation during intestinal tumorigenesis.

Mucinous intestinal tumorigenesis by *CRAD* KO

We next examined the mucinous tumour phenotype driven by *CRAD* KO. Transformation or early tumour lesions can be assessed by the development of cystic spheroid organoids instead of the normal crypt organoids[27]. Interestingly, *CRAD* KO developed the cystic spheroid, as shown in APC^{MIN} organoids (Fig. 7a).

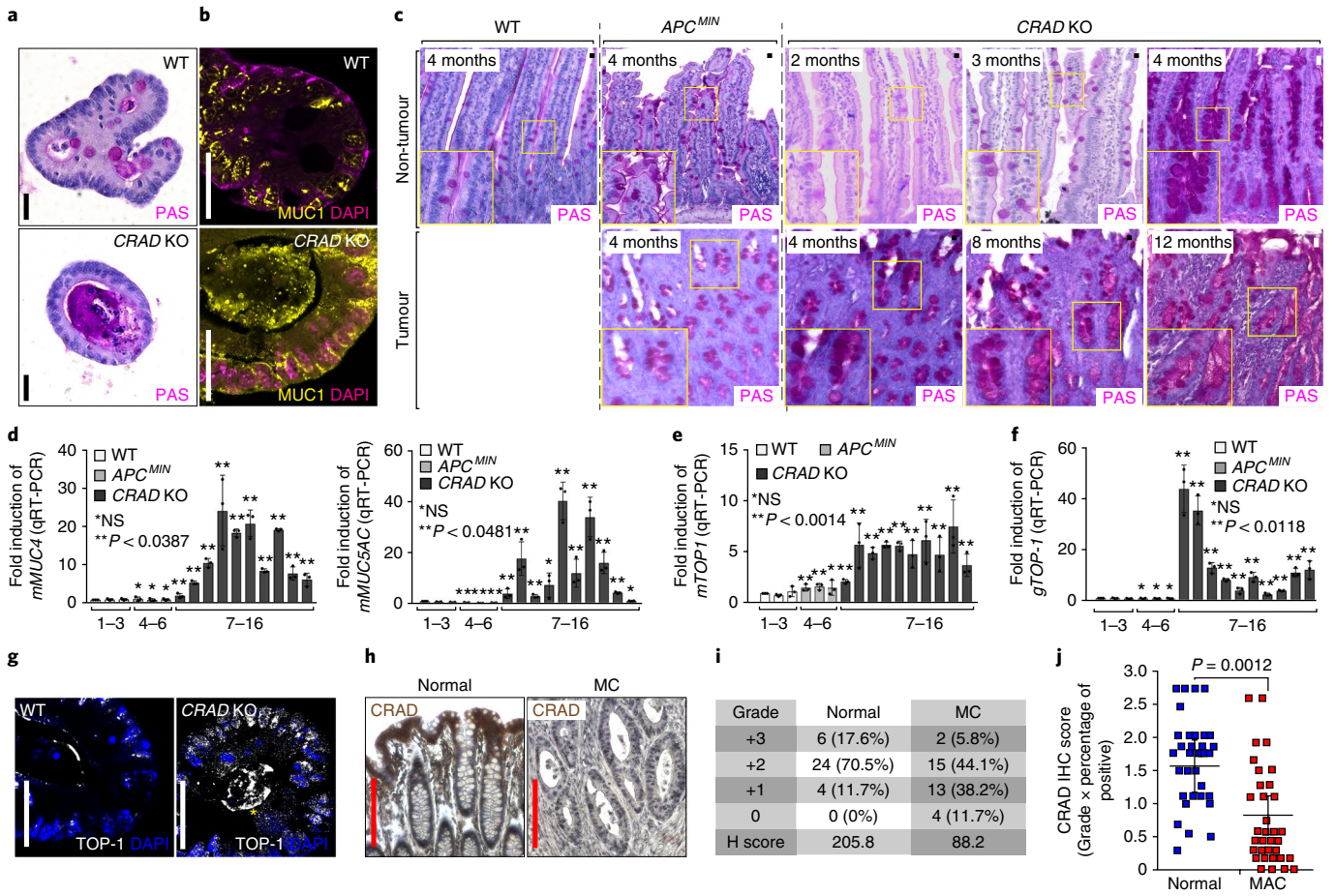

Grade	Normal	MC
+3	6 (17.6%)	2 (5.8%)
+2	24 (70.5%)	15 (44.1%)
+1	4 (11.7%)	13 (38.2%)
0	0 (0%)	4 (11.7%)
H score	205.8	88.2

Fig. 8 | Increased mucin deposition by *CRAD* KO. a,**b**, Excessive mucin deposition in *CRAD* KO-induced cystic spheroids; PAS staining (**a**) and IHC of MUC1 (**b**) was performed on organoids from WT and *CRAD* KO mice. **c**,**d**, Increased mucin deposition in *CRAD* KO-induced tumours. **c**, After fixation and paraffin embedding, each sample was PAS-stained. Yellow boxes show the magnified images. **d**, Increased mucin expression in *CRAD* KO tumours (qRT-PCR). **e**–**g**, Upregulation of *TOP-1* in *CRAD* KO tumours. WT intestine (1–3) and tumours from *APC*^{MIN} (4–6) and *CRAD* KO (7–16) mice were analysed for *TOP-1* mRNA (qRT-PCR; $n = 3$; **e**) and genomic DNA (real-time PCR; **f**). **g**, After 5 d of culture, normal crypt organoids from *CRAD* WT and spheroid organoids from *CRAD* KO were immunostained with a TOP-1 antibody. Yellow asterisk indicates artefact. **h**–**j**, CRAD inactivation in MAC patients. Immunohistochemistry of TMA with CRAD antibodies. **h**, Images are representative of 34 patient samples. **i**,**j**, After scoring CRAD expression, the H-scores (**i**) and IHC scores (**j**) were calculated ($n = 34$ for both 'normal' and MAC patient samples). The images of panels **a**–**c** and **g** are representative of three independent experiments. Data in panels **d**–**f** were obtained from three independent experiments. Red scale bars, 200 μm; error bars, mean ± s.d.; NS, not significant ($P > 0.05$); two-sided unpaired *t*-test.

CRAD KO cystic organoids exhibited increased cell proliferation (Fig. 7b and Supplementary Fig. 8a), stabilized β-catenin (Fig. 7c and Supplementary Fig. 8b), upregulated β-catenin target genes (Fig. 7d–f), disrupted actin cytoskeleton (Fig. 7g,h), abnormality of epithelial cell integrity (Fig. 7i), disorganized cell adhesion (Fig. 7j) and decreased IEC differentiation (Fig. 7k,l). *CRAD* KO cystic organoids also displayed increased mucin expression (Fig. 8a,b), as shown in *CRAD* KO tumours (see Fig. 5e,f), which indicates that *CRAD* KO upregulates mucin expression in a cell-autonomous manner. Goblet cells secrete various mucins and the number of goblet cells is elevated in MAC[28,29]. Intriguingly, the non-tumour and tumour regions of *CRAD* KO exhibited an increase in mucin expression (Fig. 8c and Supplementary Fig. 8c) and goblet cell numbers (Supplementary Fig. 8d). The marked upregulation of *mMUC* in *CRAD* KO tumours, but not in *APC*^{MIN} tumours, was confirmed through qRT-PCR (Fig. 8c and Supplementary Fig. 8e). Despite the implication of the Wnt–Notch signalling axis in goblet cell differentiation[30], only Wnt signalling target genes were upregulated by *CRAD* KO (Supplementary Fig. 6e). MAC is characterized by amplification of the *Topoisomerase-1* (*TOP-1*) allele[31]. We found that the *CRAD* KO tumours exhibited an increase in both *TOP-1* mRNA and genomic DNA levels, whereas *APC*^{MIN} tumours did not (Fig. 8e,f). *CRAD* KO tumours and cystic spheroids also showed TOP-1 upregulation (Fig. 8g and Supplementary Fig. 8f). Note that TOP-1 upregulation (2 months; Supplementary Fig. 8g) precedes mucin deposition (4 months; Fig. 8c,d and Supplementary Fig. 8c). Furthermore, IHC of MAC TMA demonstrated downregulated CRAD expression in MAC patient samples (Fig. 8h–j). Oncomine datasets also indicated that *CRAD* expression is mutually exclusive to the expression of *MUC5B* and *MUC5AC* in MAC (Supplementary Fig. 8h). These data suggest that the loss or downregulation of CRAD is associated with the development of MAC. Together, our results strongly suggest that the deletion of *CRAD* leads to the mucinous intestinal tumorigenesis.

Discussion

The mutation of *APC* in CRC causes aberrant Wnt/β-catenin signal activation. However, the β-catenin protein exhibits heterogeneous nuclear localization in the presence of homogeneous mutations in *APC*[32,33]. This 'β-catenin paradox' model[32–35] suggests that further

activation of *APC* mutation-driven Wnt signalling contributes to intestinal tumorigenesis. In epithelial cells, APC competes with E-cadherin for β-catenin binding[36], suggesting that β-catenin might also be partially sequestered by E-cadherin in the *APC*-mutated condition. Thus, it is likely that E-cadherin-mediated redistribution of β-catenin might be an additional layer limiting Wnt signalling in normal tissues.

Our study indicates that the interaction between the E-cadherin–catenin complex and the actin cytoskeleton might be a key factor suppressing tumorigenesis. Similarly, during embryogenesis, cadherin antagonizes β-catenin activity[37]. Although E-cadherin and APC might also be potential candidate regulators for the CCA complex in tumorigenesis, the E-cadherin mutation rate is meagre in CRC[38] and the function of APC is inhibited by CPs[39]. Therefore, it is plausible that the defects in other key regulators of the CCA complex might be implicated in CRC. Our findings that *CRAD* ablation-induced F-actin depolymerization leads to intestinal tumorigenesis strongly suggest that CRAD-modulated actin cytoskeletal dynamics and CCA complex stabilization play a crucial tumour suppressive role in the intestinal epithelium.

A limitation of the APC^{MIN} mouse model is that the development of intestinal adenomas mainly occurs in the small intestine and infrequently in the colorectum, unlike human CRC[25]. *CRAD* KO mice develop tumours in both the small and large intestine (Fig. 6), which recapitulates human CRC pathology. Moreover, APC^{MIN}:$CRAD^{+/-}$ mice display micro-invasion without epithelial-mesenchymal transition (EMT) (Supplementary Figs 7f,g), implying the potential roles of CRAD inactivation in CRC metastasis.

Mucinous colorectal carcinoma (10–15% of human CRC) is highly metastatic and therapeutically resistant[31]. However, the molecular mechanism of MAC development remains elusive. Tumours developed in *CRAD* KO mice display excessive mucin deposition (Figs. 5e,f, 6j,l) with *TOP-1* upregulation (Fig. 8e,f), mimicking human MAC. This is further supported by the down-regulation of CRAD in human MAC (Fig. 8h–j). Note that APC^{MIN} mice do not develop mucinous adenoma, which implies that *CRAD* loss-induced MAC development process might include distinct pathologic events in addition to Wnt/β-catenin hyperactivation. In normal intestine, mucin secreted by goblet cells is primarily involved in innate host defence. However, abnormally elevated secretion of mucin contributes to CRC progression[40]. Thus, *CRAD* inactivation might also contribute to tumorigenesis via high mucin secretion, beyond Wnt signalling. It is noteworthy that *CRAD* KO cystic organoids display mucin upregulation in a cell-autonomous manner (Fig. 8a,b), excluding the potential involvement of immunocytes in mucin expression. Given that there is no precedent MAC mouse model, our *CRAD* KO mice may be highly beneficial to studies of human MAC aetiology.

Together, the results of our study reveal that *CRAD* is a tumour suppressor and indispensable for the maintenance of epithelial cell integrity through the modulation of the cytoskeleton and thereby the CCA complex.

Online content

Any methods, additional references, Nature Research reporting summaries, source data, statements of data availability and associated accession codes are available at https://doi.org/10.1038/s41556-018-0215-z.

Received: 19 March 2018; Accepted: 17 September 2018;
Published online: 22 October 2018

References

1. Mege, R. M., Gavard, J. & Lambert, M. Regulation of cell-cell junctions by the cytoskeleton. *Curr. Opin. Cell Biol.* **18**, 541–548 (2006).
2. Gumbiner, B. M. & Kim, N. G. The Hippo-YAP signaling pathway and contact inhibition of growth. *J. Cell Sci.* **127**, 709–717 (2014).
3. Oda, H. & Takeichi, M. Evolution: structural and functional diversity of cadherin at the adherens junction. *J. Cell Biol.* **193**, 1137–1146 (2011).
4. Maiden, S. L. & Hardin, J. The secret life of alpha-catenin: moonlighting in morphogenesis. *J. Cell Biol.* **195**, 543–552 (2011).
5. Bianchini, J. M. et al. Reevaluating αE-catenin monomer and homodimer functions by characterizing E-cadherin/αE-catenin chimeras. *J. Cell Biol.* **210**, 1065–1074 (2015).
6. Edwards, M. et al. Capping protein regulators fine-tune actin assembly dynamics. *Nat. Rev. Mol. Cell Biol.* **15**, 677–689 (2014).
7. Bear, J. E. et al. Antagonism between Ena/VASP proteins and actin filament capping regulates fibroblast motility. *Cell* **109**, 509–521 (2002).
8. Xue, B. & Robinson, R. C. Guardians of the actin monomer. *Eur. J. Cell Biol.* **92**, 316–332 (2013).
9. Schafer, D. A., Jennings, P. B. & Cooper, J. A. Dynamics of capping protein and actin assembly in vitro: uncapping barbed ends by polyphosphoinositides. *J. Cell Biol.* **135**, 169–179 (1996).
10. Taoka, M. et al. V-1, a protein expressed transiently during murine cerebellar development, regulates actin polymerization via interaction with capping protein. *J. Biol. Chem.* **278**, 5864–5870 (2003).
11. George, J. et al. Comprehensive genomic profiles of small cell lung cancer. *Nature* **524**, 47–53 (2015).
12. Ambros, V. R., Chen, L. B. & Buchanan, J. M. Surface ruffles as markers for studies of cell transformation by Rous sarcoma virus. *Proc. Natl Acad. Sci. USA* **72**, 3144–3148 (1975).
13. de Curtis, I. & Meldolesi, J. Cell surface dynamics - how Rho GTPases orchestrate the interplay between the plasma membrane and the cortical cytoskeleton. *J. Cell Sci.* **125**, 4435–4444 (2012).
14. Gauthier, N. C., Masters, T. A. & Sheetz, M. P. Mechanical feedback between membrane tension and dynamics. *Trends Cell Biol.* **22**, 527–535 (2012).
15. Pollard, T. D. & Cooper, J. A. Actin, a central player in cell shape and movement. *Science* **326**, 1208–1212 (2009).
16. Bryce, N. S. et al. Cortactin promotes cell motility by enhancing lamellipodial persistence. *Curr. Biol.* **15**, 1276–1285 (2005).
17. Montross, W. T., Ji, H. & McCrea, P. D. A beta-catenin/engrailed chimera selectively suppresses Wnt signaling. *J. Cell Sci.* **113**, 1759–1770 (2000).
18. Kwiatkowski, A. V. et al. In vitro and in vivo reconstitution of the cadherin–catenin–actin complex from *Caenorhabditis elegans*. *Proc. Natl Acad. Sci. USA* **107**, 14591–14596 (2010).
19. Maiden, S. L. et al. Specific conserved C-terminal amino acids of *Caenorhabditis elegans* HMP-1/α-catenin modulate F-actin binding independently of vinculin. *J. Biol. Chem.* **288**, 5694–5706 (2013).
20. Hong, S., Troyanovsky, R. B. & Troyanovsky, S. M. Binding to F-actin guides cadherin cluster assembly, stability, and movement. *J. Cell Biol.* **201**, 131–143 (2013).
21. Braga, V. M. & Yap, A. S. The challenges of abundance: epithelial junctions and small GTPase signalling. *Curr. Opin. Cell Biol.* **17**, 466–474 (2005).
22. Tanaka, Y. et al. Frequent β-catenin mutation and cytoplasmic/nuclear accumulation in pancreatic solid-pseudopapillary neoplasm. *Cancer Res.* **61**, 8401–8404 (2001).
23. Peterson, L. W. & Artis, D. Intestinal epithelial cells: regulators of barrier function and immune homeostasis. *Nat. Rev. Immunol.* **14**, 141–153 (2014).
24. van Es, J. H. et al. Wnt signalling induces maturation of Paneth cells in intestinal crypts. *Nat. Cell Biol.* **7**, 381–386 (2005).
25. Moser, A. R., Pitot, H. C. & Dove, W. F. A dominant mutation that predisposes to multiple intestinal neoplasia in the mouse. *Science* **247**, 322–324 (1990).
26. Bara, J., Forgue-Lafitte, M. E., Maurin, N., Flejou, J. F. & Zimber, A. Abnormal expression of gastric mucin in human and rat aberrant crypt foci during colon carcinogenesis. *Tumour Biol.* **24**, 109–115 (2003).
27. Sachs, N. & Clevers, H. Organoid cultures for the analysis of cancer phenotypes. *Curr. Opin. Genet. Dev.* **24**, 68–73 (2014).
28. Podolsky, D. K., Fournier, D. A. & Lynch, K. E. Human colonic goblet cells. Demonstration of distinct subpopulations defined by mucin-specific monoclonal antibodies. *J. Clin. Invest.* **77**, 1263–1271 (1986).
29. Yamachika, T. et al. Establishment and characterization of a human colonic mucinous carcinoma cell line with predominant goblet-cell differentiation from liver metastasis. *Pathol. Int.* **55**, 550–557 (2005).
30. van Es, J. H. et al. Notch/gamma-secretase inhibition turns proliferative cells in intestinal crypts and adenomas into goblet cells. *Nature* **435**, 959–963 (2005).
31. Hugen, N., Brown, G., Glynne-Jones, R., de Wilt, J. H. & Nagtegaal, I. D. Advances in the care of patients with mucinous colorectal cancer. *Nat. Rev. Clin. Oncol.* **13**, 361–369 (2016).
32. Brabletz, T. et al. Nuclear overexpression of the oncoprotein beta-catenin in colorectal cancer is localized predominantly at the invasion front. *Pathol. Res. Pract.* **194**, 701–704 (1998).
33. Vermeulen, L. et al. Wnt activity defines colon cancer stem cells and is regulated by the microenvironment. *Nat. Cell Biol.* **12**, 468–476 (2010).

34. Goentoro, L. & Kirschner, M. W. Evidence that fold-change, and not absolute level, of beta-catenin dictates Wnt signaling. *Mol. Cell* **36**, 872–884 (2009).
35. Voloshanenko, O. et al. Wnt secretion is required to maintain high levels of Wnt activity in colon cancer cells. *Nat. Commun.* **4**, 2610 (2013).
36. Hulsken, J., Birchmeier, W. & Behrens, J. E-cadherin and APC compete for the interaction with beta-catenin and the cytoskeleton. *J. Cell Biol.* **127**, 2061–2069 (1994).
37. Fagotto, F., Funayama, N., Gluck, U. & Gumbiner, B. M. Binding to cadherins antagonizes the signaling activity of beta-catenin during axis formation in *Xenopus*. *J. Cell Biol.* **132**, 1105–1114 (1996).
38. Brannon, A. R. et al. Comparative sequencing analysis reveals high genomic concordance between matched primary and metastatic colorectal cancer lesions. *Genome Biol.* **15**, 454 (2014).
39. Okada, K. et al. Adenomatous polyposis coli protein nucleates actin assembly and synergizes with the formin mDia1. *J. Cell Biol.* **189**, 1087–1096 (2010).
40. Kufe, D. W. Mucins in cancer: function, prognosis and therapy. *Nat. Rev. Cancer* **9**, 874–885 (2009).

Acknowledgements

We thank J.A. Cooper for his insightful comments and recommendations regarding the experiment and result analysis. We thank S.-H. Lee, H.N. Suh, S.H. Lee and K.-S. Park for helpful comments on the manuscript. This work was supported by the Cancer Prevention Research Institute of Texas (grant no. RP140563 to J-.I.P.), the National Institutes of Health (grant nos R01 CA193297-01 (to J-.I.P.), 5R01 GM107079 (to P.D.M.) and R01 GM126048 (to W.W.)), the Department of Defense Peer Reviewed Cancer Research Program (grant no. CA140572 to J-.I.P.), a Duncan Family Institute for Cancer Prevention and Risk Assessment Grant (IRG-08-061-01; to J-.I.P.), a Center for Stem Cell and Developmental Biology Transformative Grant (MD Anderson Cancer Center to J-.I.P.), an Institutional Research Grant (MD Anderson Cancer Center; to J-.I.P.), a New Faculty Award (MD Anderson Cancer Center Support Grant; to J-.I.P.), a Metastasis Research Center Grant (MD Anderson; to J-.I.P.) and a Uterine SPORE Career Enhancement Program (MD Anderson; to J-.I.P.). The core facility (DNA sequencing and Genetically Engineered Mouse Facility) was supported by the MD Anderson Cancer Center Support Grant (CA016672).

Author contributions

Y.-S.J. and J.-I.P. conceived the experiments. Y.-S.J., W.W., S.J., J.Z., M.S., M.J.K., E.M.L., J.S. and J.-I.P. performed the experiments. Y.-S.J., J.C., P.D.M., S.Z. and J.-I.P. analysed the data. Y.-S.J. and J.-I.P. wrote the manuscript.

Competing interests

The authors declare no competing interests.

Additional information

Supplementary information is available for this paper at https://doi.org/10.1038/s41556-018-0215-z.

Reprints and permissions information is available at www.nature.com/reprints.

Correspondence and requests for materials should be addressed to J.-I.P.

Publisher's note: Springer Nature remains neutral with regard to jurisdictional claims in published maps and institutional affiliations.

Methods

In silico analysis of CRAD expression and genetic alteration. The expression of *CRAD* in CRC cells was analysed in cBioportal (www.cbioportal.org), Oncomine (www.oncomine.org), COSMIC (https://cancer.sanger.ac.uk/cosmic) and the GEO database (www.ncbi.nlm.nih.gov/geo)[41–44]. The cBioportal analysis was performed with default options using the TCGA (2012 and provisional) and Genentech (2012) datasets for gene alterations (mutations and copy number change) and gene expression (RNA-Seq reads per kilobase million)[45]. For Oncomine analysis, the following options were chosen: $P < 0.05$, gene rank < 1%, and fold change > 2. The COSMIC analysis was performed using default options in the large intestinal carcinoma tissue. The accession number GDS2947 with probes 227231_at and 227230_s_at was selected for GEO analysis.

Mammalian cell culture. All cell lines were purchased from the American Type Culture Collection (ATCC). KM12, HCT15, HT29, HCT116, COLO205, SW620, HCC2998 and 293T cells were maintained in Dulbecco's modified Eagle's medium (DMEM; Corning) containing 10% fetal bovine serum (FBS; HyClone). FHC cells were maintained in DMEM/F-12 (Invitrogen) containing 10% FBS, cholera toxin (10 ng ml^{-1}; Sigma), insulin (5 µg ml^{-1}; Sigma), transferrin (5 µg ml^{-1}; Fisher) and hydrocortisone (100 ng ml^{-1}; Sigma). CCD-841CoN, LS-174T and RKO cells were maintained in Eagle's Minimum Essential Medium (ATCC) containing 10% FBS. DLD-1 and NCI-H508 cells were maintained in RPMI1640 medium (Corning) containing 10% FBS. Mycoplasma contamination was tested for using the MycoAlert mycoplasma detection kit (Lonza). Lentiviral plasmids encoding shRNAs for CRAD (Dharmacon; V3LHS _367333; _367334; _367337) or retroviral plasmids were packed in 293T cells and were stably transduced into target cells using puromycin (2 µg ml^{-1}; Sigma) and hygromycin B (2 µg ml^{-1}; Fisher) selection, respectively. For transient transfection, pcDNA3.1 mammalian expression plasmids were used. CK-666 (Fisher), iCRT14 (Santa Cruz), Jasplakinolide (Sigma), Cytochalasin D (Sigma) and Latrunculin B (Sigma) were used for cell treatment.

Constructs. All constructs were generated from cDNA of open reading frame sources through PCR and ligated into mammalian expression plasmids or retroviral vector plasmids (FLAG-pcDNA3.1 and HA-pWZL). The CARMIL1, Δ CPI and M1–M4 CRAD mutants were constructed using PCR-based mutagenesis. Immunoblotting was used to test for the depletion of endogenous *CRAD* expression in three different lentiviral plasmids encoding shCRADs. All of the constructs were verified through DNA sequencing. The primer sequences can be found in the 'Primer information' section.

Gene expression analysis. Cells were lysed with TRIzol reagent (Invitrogen) to extract RNA. The RNA (1 µg) was then reverse transcribed using iScript RT supermix for RT-qPCR (Biorad). The resulting cDNAs were used for gene expression analysis by means of qRT-PCR (StepOnePlus; Applied Biosystems). *HPRT1* was used as an internal control for normalization. Fold induction was quantified using the $2^{-\Delta\Delta Ct}$ method. The primer sequences can be found in the 'Primer information' section.

Immunoblotting and immunoprecipitation. Whole-cell lysates of mammalian cells were prepared by incubating cells with NP-40 lysis buffer (0.5% NP-40, 1.5 mM $MgCl_2$, 25 mM HEPES, 150 mM KCl, 10% glycerol, 1 mM phenylmethylsulfonyl fluoride, 12.7 mM benzamidine HCl, 0.2 mM aprotinin, 0.5 mM leupeptin and 0.1 mM pepstatin A) for 20 min at 4 °C followed by centrifugation (13,148 g for 10 min). The supernatants were denatured with 5× SDS sample buffer (200 mM Tris-HCl pH 6.8, 40% glycerol, 8% SDS, 200 mM dithiothreitol and 0.08% bromophenol blue) at 95 °C for 5 min followed by SDS–poylacrylamide electrophoresis (SDS-PAGE). For immunoblot blocking and antibody incubation, 0.1% non-fat dry milk in Tris-buffered saline and Tween-20 (25 mM Tris-HCl pH 8.0, 125 mM NaCl and 0.5% Tween-20) was used. SuperSignal West Pico (Thermo Scientific) and Femto (Thermo Scientific) reagents were used to detect horseradish peroxidase-conjugated secondary antibodies. For immunoprecipitation, cell lysates were incubated with 20 µl anti-FLAG M2 magnetic beads (Sigma) for 2 h. The immunoprecipitates were then washed three times with cell lysis buffer, eluted with SDS sample buffer and analysed by means of immunoblotting. The antibodies that were used for immunoblotting and immunoprecipitation can be found in the 'Antibody information' section.

IHC and immunofluorescent staining. Human CRC TMA was purchased from Biomax and immunostained with anti-CRAD antibodies, as previously reported[41–44]. For the immunostaining of tumour samples from xenograft transplantation and intestinal tissues, samples were collected and fixed in 10% formalin. After processing for paraffin embedding, the sectioned samples were immunostained according to the standard protocol: deparaffinization, blocking and incubation with primary and fluorescence-conjugated secondary antibodies. Images were captured using fluorescent or confocal microscopes (Zeiss Observer and LSM880) and AxioVision and Zen software, respectively. The antibodies used for IHC can be found in antibody information.

In vitro actin polymerization and F-/G-actin fractionation assays. Cell and intestinal tissue extracts were subjected to in vitro actin polymerization and F-/G-actin fractionation assays using the actin polymerization (Cytoskeleton Inc.) and F-/G-actin fractionation (Cytoskeleton Inc.) kits, respectively, as per the manufacturer-provided protocol.

Reporter assays. The reporter plasmids pMegaTOPFLASH and pMegaFOPFLASH were transiently transfected with pSV40-Renilla (an internal control), as previously performed[46].

Mass spectrometry. Cells were grown in twenty 10 cm dishes until they reached 80% confluence. Cells were then transfered to a 250 ml centrifuge bottle (Corning) for harvesting, centrifuged at 300 g for 5 min at 4 °C; the cell pellets were suspended in 30 ml PBS and centrifugation was repeated under the same conditions. The cells were then incubated with 10–15 ml ice-cold NETN buffer (20 mM Tris-HCl pH 8.0, 100 mM NaCl, 0.5 mM EDTA and 0.5%(v/v) Nonidet P-40; containing freshly added proteinase and phosphatase inhibitors) on a shaker at 4 °C for 20 min. The lysates were centrifuged at 4 °C and 13,148 g for 15 min. Transferred supernatants were incubated with streptavidin-conjugated beads (Amersham) for 1 h at 4 °C. After three washes with NETN buffer, the beads were transferred to a new tube and interacting proteins were eluted by incubating with 1.5 ml NETN buffer containing 2 mg ml^{-1} biotin (Sigma) for about 90 min at 4 °C. The eluted proteins were transferred and incubated with S protein beads (Novagen) for 1 h. The beads were subjected to SDS-PAGE after three washes. The protein bands were excised and subjected to mass spectrometry analysis.

The excised gel bands were cut into pieces approximately 1 mm^3 in size and in-gel trypsin digestion was performed. Dried samples were reconstituted in 5 µl HPLC solvent A (2.5% acetonitrile and 0.1% formic acid). Through packing 5 µm C18 spherical silica beads into a fused silica capillary (100 µm inner diameter × ~20 cm length) with a flame-drawn tip, a nanoscale reverse-phase HPLC capillary column was created. After equilibrating the column, each sample was loaded onto the column with a Famos autosampler (LC Packings) and peptides were eluted with increasing concentrations of solvent B (97.5% acetonitrile and 0.1% formic acid). The eluted peptides were subjected to electrospray ionization and then entered into an LTQ Velos ion-trap mass spectrometer (ThermoFisher). After the detection, isolation and fragmentation of peptides to produce a tandem mass spectrum of specific fragment ions for each peptide, the peptide sequences were determined by matching protein databases (The human IPI database version 3.6) with the acquired fragmentation pattern by the software program SEQUEST (version 28; ThermoFisher). The specificity of the enzyme was set to partially tryptic with two missed cleavages. Carboxyamidomethyl (cysteines, fixed) and oxidation (methionine, variable) are included in the modification. Mass tolerance was set to 2.0 for precursor ions and 1.0 for fragment ions. For a false discovery rate lower than 1% at the peptide level, spectral matches were filtered based on the target-decoy method[47]. Lastly, only tryptic matches were reported and spectral matches were manually examined. Matched peptides to multiple proteins were assigned so that only the most logical protein was included (Occam's razor).

Duolink assays. For the visualization of protein interaction in situ, cells were seeded onto cover glass. After fixation with 4% formalin for 5 min, cells were permeabilized with 0.01% Triton X-100 for Duolink assays (Sigma), which were performed as per the manufacturer's recommended protocol: blocking, primary antibody reaction, positive and negative probe reaction, ligation, polymerization and amplification.

Xenograft transplantation assays. Nude mice (BALB/c nude) (4 months old) were purchased from the Institutional Veterinary Medicine and Surgery Facility. Each mouse ($n = 10$) was subcutaneously injected with 1×10^7 cells into the left flank (HCT116 (control)) and the right flank (HCT116-CRAD). Fifteen days after transplantation, tumours were harvested to assess tumour weight and IHC.

***CRAD* KO mice.** The KO mice were generated using clustered regularly interspaced short palindromic repeats (CRISPR). *Cas9* mRNA was purchased from Sigma Aldrich and gBlock of guide RNA (gRNA) was designed (gRNA sequence: 5′ TTCATGGGAATGGCGTTCGATGG 3′ and 5′ CAGCACAGATGCTAGCTCAGAGG 3′), based on the protospacer adjacent motif (PAM) on the target site. The gRNA was transcribed using SureGuide gRNA Synthesis Kit (Agilent). The *Cas9* mRNA and gRNA were injected into the pronucleus of the C57BL/B6 blastocysts to generate *CRAD* KO mice at the genetically engineered mouse facility at the MD Anderson Cancer Center. *CRAD* KO pups from eight independent founder strains were utilized for analysis. *CRAD* KO was confirmed by immunoblotting, immunofluorescence and genomic DNA sequencing. All mice were maintained according to institutional guidelines and Association for Assessment and Accreditation of Laboratory Animal Care International standards (IACUC00001140; University of Texas MD Anderson Cancer Center Institutional Animal Care and Use Committee). The study is compliant with all relevant ethical regulations regarding animal research.

Cell proliferation assays. Fourteen days after seeding, the cells were fixed with 4% formalin and stained with crystal violet (Fisher) for 30 min. Once the samples were completely dry, images were taken. For quantification, cells stained with crystal

violet were lysed with 10% SDS and absorbances at 590 nm were measured using a 96-well microplate reader (BioTek microplate reader). In addition, the number of cells was counted using a hemocytometer as an indication of growth days.

Uncapped barbed end detection. Cells were seeded onto cover glass for the detection of uncapped barbed ends. After serum starvation for 30 min, cells were stimulated with serum for 1 min and permeabilized with saponin buffer (20 mM HEPES, 138 mM KCl, 4 mM $MgCl_2$, 3 mM EGTA, 0.2 mg ml^{-1} saponin, 1% BSA, 1 mM ATP and 3 µM phalloidin) for 1 min, as reported previously[48]. The cells were then washed with saponin-free buffer and the uncapped barbed ends were labelled with the addition of 0.4 uM Alexa-488-actin for 3 min at 37 °C. After 4% paraformaldehyde fixation, cells were stained with phalloidin. Labelled uncapped barbed ends were monitored with a Super Resolution microscope (LSM880 Airyscan; Zeiss).

Recombinant protein purification. To express proteins, bacterial cells were transformed with the appropriate expression vectors, induced with the addition of 1 mM isopropylthiogalactoside at absorbance (600 nm) = 0.8 and incubated at 37 °C for 4 h. The cells were then harvested and extracts were prepared by sonication in 1×NETN extraction buffer containing protease inhibitors. The clarified extracts were incubated with Glutathione Sepharose 4B as per manufacturer's instructions (GE Healthcare). For the purification of proteins, the pellet was sonicated twice. The beads were washed three times with 1×NETN buffer. Proteins were eluted by incubating the beads overnight at 4 °C with PreScission Protease (GE Healthcare) in buffer (50 mM Tris-HCl pH 7.0, 150 mM NaCl, 1 mM EDTA and 1 mM dithiothreitol). The purity of proteins was analysed by SDS-PAGE and samples were stored at −80 °C.

Organoids culture. As per earlier work[49], we isolated and maintained crypt organoids in organoid culture Advanced DMEM/F12 medium (Invitrogen) containing growth factors (50 ng ml^{-1} EGF (Peprotech), 500 ng ml^{-1} R-spondin (R&D), 100 ng ml^{-1} Noggin (Peprotech) and 10 µM Y-27632 (Sigma)). Spheroid organoids were maintained in crypt organoid culture Advanced DMEM/F12 medium without R-spondin. After 5 d of crypt/spheroid organoid formation, the organoids were collected and fixed in 10% formalin for IHC.

TMA analysis. After pathological analysis (grade and percentage of CRAD expression in TMA (normal versus MAC)) was completed as per previous studies[16,50], the H-score was calculated using the following formula: 1 × (% cells 1+) + 2 × (% cells 2+) + 3 × (% cells 3+).

Protein purification. Protein purification using TnT Quick Coupled Transcription/Translation System (Promega), which provides eukaryotic cell-free protein expression, was performed according to the manufacturer's protocol. Purified proteins do not contain other actin-related proteins.

Primer information. See Supplementary Table 4 for a complete list of primers.

Antibody information. See Supplementary Table 5 for a complete list of antibodies.

Statistics and reproducibility. Student's *t*-test was used for comparisons between two groups ($n \geq 3$). *P* values smaller than 0.05 were considered significant. Error bars indicate standard deviation. All experiments were performed three or more times with similar results, independently under identical or similar conditions, except the experiments shown in Fig. 2g, Supplementary Fig. 2c,d,p, 6f,g and 8c, which were performed twice and the experiments in Figs. 1c, 2j, 4k, 5d and 7a, which were performed once.

Reporting Summary. Further information on research design is available in the Nature Research Reporting Summary linked to this article.

Data availability

Microarray data that support the findings of this study have been deposited in GEO (accession code GDS2947). Mass spectrometry data used in this study is available from Supplementary Table 2. The CRAD expression data in CRC cells were derived from the cBioportal using the TCGA Research Network (http://cancergenome.nih.gov/) and Genetech datesets. The dataset derived from this resource that supports the findings of this study is available in Oncomine (https://www.oncomine.org/resource). CRAD expression data were also derived from cBioportal (http://www.cbioportal.org/) and COSMIC database (https://cancer.sanger.ac.uk/cosmic). Source data for Figs. 1–8 and Supplementary Figs. 1–8 have been provided as Supplementary Table 4. All other data supporting the findings of this study are available from the corresponding author on reasonable request.

References

41. Edgar, R., Domrachev, M. & Lash, A. E. Gene Expression Omnibus: NCBI gene expression and hybridization array data repository. *Nucleic Acids Res.* **30**, 207–210 (2002).
42. Forbes, S. A. et al. COSMIC: mining complete cancer genomes in the Catalogue of Somatic Mutations in Cancer. *Nucleic Acids Res.* **39**, D945–D950 (2011).
43. Gao, J. et al. Integrative analysis of complex cancer genomics and clinical profiles using the cBioPortal. *Sci. Signal.* **6**, pl1 (2013).
44. Rhodes, D. R. et al. ONCOMINE: a cancer microarray database and integrated data-mining platform. *Neoplasia* **6**, 1–6 (2004).
45. Cerami, E. et al. The cBio cancer genomics portal: an open platform for exploring multidimensional cancer genomics data. *Cancer Discov.* **2**, 401–404 (2012).
46. Jung, H. Y. et al. PAF and EZH2 induce Wnt/β-catenin signaling hyperactivation. *Mol. Cell* **52**, 193–205 (2013).
47. Jun, S. et al. PAF-mediated MAPK signaling hyperactivation via LAMTOR3 induces pancreatic tumorigenesis. *Cell Rep.* **5**, 314–322 (2013).
48. Elias, J. E. & Gygi, S. P. Target-decoy search strategy for increased confidence in large-scale protein identifications by mass spectrometry. *Nat. Methods* **4**, 207–214 (2007).
49. Sato, T. et al. Single Lgr5 stem cells build crypt-villus structures in vitro without a mesenchymal niche. *Nature* **459**, 262–265 (2009).
50. Symons, M. H. & Mitchison, T. J. Control of actin polymerization in live and permeabilized fibroblasts. *J. Cell Biol.* **114**, 503–513 (1991).

nature research

Corresponding author(s): Jae-Il Park

Reporting Summary

Nature Research wishes to improve the reproducibility of the work that we publish. This form provides structure for consistency and transparency in reporting. For further information on Nature Research policies, see Authors & Referees and the Editorial Policy Checklist.

Statistical parameters

When statistical analyses are reported, confirm that the following items are present in the relevant location (e.g. figure legend, table legend, main text, or Methods section).

n/a	Confirmed	
☐	☒	The exact sample size (*n*) for each experimental group/condition, given as a discrete number and unit of measurement
☐	☒	An indication of whether measurements were taken from distinct samples or whether the same sample was measured repeatedly
☐	☒	The statistical test(s) used AND whether they are one- or two-sided *Only common tests should be described solely by name; describe more complex techniques in the Methods section.*
☒	☐	A description of all covariates tested
☐	☒	A description of any assumptions or corrections, such as tests of normality and adjustment for multiple comparisons
☐	☒	A full description of the statistics including central tendency (e.g. means) or other basic estimates (e.g. regression coefficient) AND variation (e.g. standard deviation) or associated estimates of uncertainty (e.g. confidence intervals)
☐	☒	For null hypothesis testing, the test statistic (e.g. *F*, *t*, *r*) with confidence intervals, effect sizes, degrees of freedom and *P* value noted *Give P values as exact values whenever suitable.*
☒	☐	For Bayesian analysis, information on the choice of priors and Markov chain Monte Carlo settings
☒	☐	For hierarchical and complex designs, identification of the appropriate level for tests and full reporting of outcomes
☐	☒	Estimates of effect sizes (e.g. Cohen's *d*, Pearson's *r*), indicating how they were calculated
☐	☒	Clearly defined error bars *State explicitly what error bars represent (e.g. SD, SE, CI)*

Our web collection on statistics for biologists may be useful.

Software and code

Policy information about availability of computer code

Data collection	No software was used for data collection.
Data analysis	The human IPI databases version 3.6 (determination of peptide sequences) and SEQUEST ver.28 (fragmentation patterning) are used for analysis of mass spectrometry result. All statistical analyses and plots were generated using GraphPad Prism 7. Correlation analysis was conducted in R. Heatmap was generated with the GraphPad Prism 7. Images were analyzed using AxioVision and Zen software.

For manuscripts utilizing custom algorithms or software that are central to the research but not yet described in published literature, software must be made available to editors/reviewers upon request. We strongly encourage code deposition in a community repository (e.g. GitHub). See the Nature Research guidelines for submitting code & software for further information.

Data

Policy information about availability of data

All manuscripts must include a data availability statement. This statement should provide the following information, where applicable:

- Accession codes, unique identifiers, or web links for publicly available datasets
- A list of figures that have associated raw data
- A description of any restrictions on data availability

Microarray data that support the findings of this study have been deposited in the Gene Expression Omnibus (GEO) under accession code GDS2947. Mass

spectrometry data used in this study is available from Supplementary Table 2. The CRAD expression data in CRC cells were derived from the cBioportal using the TCGA Research Network: http://cancergenome.nih.gov/ and Genetech datesets. The data-set derived from this resource that supports the findings of this study is available in Oncomine (https://www.oncomine.org/resource). CRAD expression data were also derived from cBioportal (http://www.cbioportal.org/) and COSMIC database (Catalogue of Somatic Mutations in Cancer) (https://cancer.sanger.ac.uk/cosmic). Source data for Figs. 1-8 and Supplementary Figs. 1-8 have been provided as Supplementary Table 4. All other data supporting the findings of this study are available from the corresponding author on reasonable request.

Field-specific reporting

Please select the best fit for your research. If you are not sure, read the appropriate sections before making your selection.

☒ Life sciences ☐ Behavioural & social sciences ☐ Ecological, evolutionary & environmental sciences

For a reference copy of the document with all sections, see nature.com/authors/policies/ReportingSummary-flat.pdf

Life sciences study design

All studies must disclose on these points even when the disclosure is negative.

Sample size	For animal studies, sample size was estimated by power calculation, as following; Using StatsToDo software (http://www.statstodo.com/SSiz2Means_Pgm.php; alpha level P=0.05; power 80%; expected background standard deviation=0.5; difference between two means to be detected=0.5).
Data exclusions	No samples or animals were excluded. Also, the criteria were not pre-established in experiments.
Replication	All experiments were performed using at least three biological replicas unless specified. All experiments were successfully replicated.
Randomization	Tumor-bearing and genetic engineered animals in tumorigenesis studies were examined in certain aged groups (3-12 months of age) for determine the tumor suppressive effect.
Blinding	Yes. Blinding was used for all analyses.

Reporting for specific materials, systems and methods

Materials & experimental systems

n/a	Involved in the study
☒	☐ Unique biological materials
☐	☒ Antibodies
☐	☒ Eukaryotic cell lines
☒	☐ Palaeontology
☐	☒ Animals and other organisms
☒	☐ Human research participants

Methods

n/a	Involved in the study
☒	☐ ChIP-seq
☒	☐ Flow cytometry
☒	☐ MRI-based neuroimaging

Antibodies

Antibodies used	See Supplementary Table 5
Validation	All antibodies used were validated by the respective commercial source for the application used in this manuscript.

Eukaryotic cell lines

Policy information about cell lines

Cell line source(s)	All cell lines were purchased from American Type Culture Collection (ATCC). KM12, HCT15, HT29, HCT116, COLO205, SW620, HCC2998, and 293T cells were maintained in Dulbecco's modified Eagle's medium (DMEM; Corning; 10-013-CV) containing 10% fetal bovine serum (FBS; Hyclone; SH3.007.003). FHC cell was maintained in DMEM: F-12 (Invitrogen; 11330-032) containing 10% FBS, cholera toxin (10ng/ml; Sigma; C-8052), insulin (5µg/ml; Sigma; I-1882), transferrin (5µg/ml; Fisher; 354204), and hydrocortisone (100ng/ml; Sigma; H-0008). CCD-841CoN, LS-174T, and RKO cells were maintained in Eagle's Minimum Essential Medium (EMEM; ATCC; 30-2003) containing 10% FBS. DLD-1 and NCI-H508 cells were maintained

	RPMI1640 (Corning; 10-049-CMR) containing 10% FBS. Mycoplasma contamination was examined using MycoAlert mycoplasma detection kit (Lonza; LT07-218).
Authentication	None of the cell lines were authenticated.
Mycoplasma contamination	All cell lines tested were negative for mycoplasma contamination
Commonly misidentified lines (See ICLAC register)	No commonly misidentified lines were used.

Animals and other organisms

Policy information about studies involving animals; ARRIVE guidelines recommended for reporting animal research

Laboratory animals	C57BL/B6 mice (wildtype, APCmin, and CRAD KO), both gender, 3-12months of age, determination of tumorigenesis BALB/c nude mice, male, 4 months of age, xenograft
Wild animals	The study did not involve wild animals.
Field-collected samples	The study did not involve field-collected samples.